Electronic Supplementary Material (ESI) for ChemComm.

Supplementary Information

Amphiphile desymmetrisation-induced steric relief governs self-assembly pathways in aqueous media

Nils Bäumer,[a,b] Soichiro Ogi,[b] Lorenz Borsdorf,[a] Shigehiro Yamaguchi,[b,c,*] Gustavo Fernández[a,*]

[a] Organisch-Chemisches Institut, Westfälische Wilhelms-Universität Münster, Corrensstraße 36, 48149 Münster, Germany. e-mail: fernandg@uni-muenster.de

[b] Department of Chemistry, Graduate School of Science, and Integrated Research Consortium on Chemical Science (IRCCS), Nagoya University, Furo, Chikusa, Nagoya 464-8602, Japan.

[c] Institute of Transformative Bio-Molecules (WPI-ITbM), Nagoya University, Furo, Chikusa, Nagoya 464-8602, Japan. e-mail: yamaguchi@chem.nagoya-u.ac.jp

Table of Contents

Materials and Methods

General

^{1}H and ^{13}C NMR spectra were recorded with a JEOL AL-400 spectrometer (400 MHz for ^{1}H, 100 MHz for ^{13}C) or JEOL JNM-ECS400 (400 MHz for ^{1}H, 100 MHz for ^{13}C) in $CDCl_3$. The chemical shifts in ^{1}H NMR spectra are reported in δ ppm using the residual protons of the solvent as an internal standard ($CHCl_3$ δ 7.26), and those in ^{13}C NMR spectra are reported using the solvent signal as an internal standard ($CHCl_3$ δ 77.16). Mass spectra were measured with a Thermo Fisher Scientific Exactive Plus Orbitrap MS System with the ionization methods of electrospray ionization (ESI). Thin layer chromatography (TLC) was performed on glass plates coated with 0.25 mm thickness of silica gel $60F_{254}$ (Merck). Column chromatography was performed in self-packed columns using silica gel PSQ100B (Fuji Silysia Chemicals). Preparative Gel permeation Chromatography (GPC) was performed using LC-918 (Japan Analytical Industry) equipped with gel column (JAIGEL-2.5H and -3H) using $CHCl_3$ as eluent. All chemicals were purchased from commercial suppliers and used without further purification. Anhydrous THF was purchased from Kanto Chemicals and further purified by Glass Contour Solvent Systems.

UV/Vis spectroscopy

The spectroscopic measurements were conducted under ambient conditions using solvents of spectroscopic grade. UV/Vis absorption spectra were recorded using quartz cuvettes of 1 cm path length with a JASCO V-750 and a V-770 spectrophotometer equipped with a JASCO ETCR-762 cell holder for temperature control.

Photoluminescence spectroscopy

Fluorescence spectra were recorded using quartz cuvettes of 1 cm path length with a JASCO FP-8500 spectrometer.

Dynamic and static light scattering

DLS spectra were recorded on a Malvern Zetasizer NANO ZS, equipped with a 4 mW He-Ne laser. Additional DLS and SLS spectra have been recorded on a *CGS-3 Compact Goniometer System* manufactured by *ALV GmbH*, equipped with a HeNe Laser with a wavelength of 632.8 nm (22 mW) and an *ALV/LSE-5004 Digital Correlator* by *ALV GmbH*.

Transmission electron microscopy

TEM was performed with a JEM-1400EM (JEOL) using an acceleration voltage of 80 kV. The samples (10 µL) were drop-casted on a carbon-coat copper grid (400 mesh) and the solvent was removed with a filter paper, followed by drying under reduced pressure for no less than 12 hours. The measurements were conducted without additional staining.

Scanning electron microscopy

The SEM images were recorded on a Phenom ProX Desktop SEM manufactured by Thermo Fisher Scientific. The individual images have been recorded using a zoom between 37000× and 13000× with a BSD detector and an acceleration voltage of 5 kV (For individual images please see the corresponding figure caption).

Atomic force microscopy

The AFM images have been recorded on a Multimode®8 SPM System manufactured by Bruker AXS. The used cantilevers were AC200TS by Oxford Instruments with an average spring constant of 9 N m^{-1}, an average frequency of 150 kHz, an average length of 200 µm, an average width of 40 µm and an average tip radius of 7 nm.

Synthetic Details and Characterization

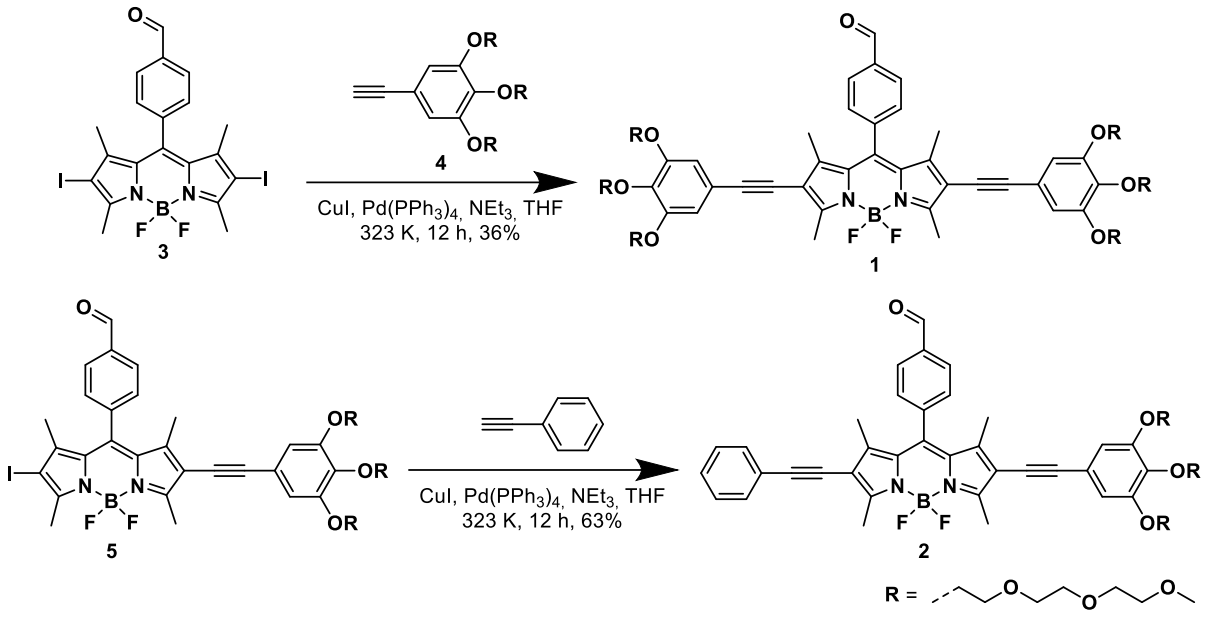

Scheme S1: Synthetic scheme for the preparation of **1** and **2**. Compounds **3**, **4** and **5** were prepared in accordance with previous reports and showed identical spectroscopic properties as those described in the literature.[1,2]

Compound **1**

Compound **3** (67 mg, 0.11 mmol, 1 eq.); CuI (2 mg) and $Pd(PPh_3)_4$ (10 mg) were dissolved in a mixture of distilled THF and NEt_3 (15 mL, 1:1, v/v) and stirred at room temperature under a nitrogen atmosphere for 40 minutes. Compound **4** (137 mg, 0.23 mmol, 2.1 eq.) dissolved in distilled THF (8 mL) was added slowly. Afterwards the reaction mixture was heated to 323 K and stirred for 12 hours. After cooling to room temperature, the solvent was removed under vacuum and the crude product was purified by column chromatography (SiO_2, DCM/MeOH 9:1) and GPC ($CHCl_3$) to give compound **1** as a highly viscous purple oil.

Yield: 58 mg, 0.04 mmol, 36%.

^{1}H NMR (298 K, 400 MHz, $CDCl_3$): δ = 10.14 (s, 1H); 8.08 (d, *J* = 8.1 Hz, 2H); 7.53 (d, *J* = 8.1 Hz, 2H); 6.67 (s, 4H); 4.16-4.11 (m, 12 H); 3.85-3.82 (m, 8H); 3.79-3.76 (m, 4H); 3.73-3.69 (m, 12 H); 3.66-3.61 (m, 24H); 3.54-3.51 (m, 12H); 3.37-3.35 (m, 18H); 2.71 (s, 6H); 1.49 (s, 6H) ppm.

^{13}C NMR: (298 K, 100 MHz, $CDCl_3$): δ = 191.4, 159.1, 152.5, 143.4, 140.7, 140.2, 139.4, 136.9, 130.6, 130.5, 129.1, 118.0, 116.6, 111.1, 96.8, 83.4, 80.3, 77.3, 72.5, 72.0, 71.9, 70.8, 70.7, 70.6, 70.5, 70.5, 69.6, 68.9, 59.0, 13.9, 13.7 ppm. (note that between δ = 71.0 and 70.5 ppm multiple signals corresponding to the glycol chains overlap, preventing a clear identification of all peaks)

HR-MS (ESI in MeOH/$CHCl_3$): *m/z* calculated for $[M+2Na]^{2+}$ = 785.36658; found = 785.36670.

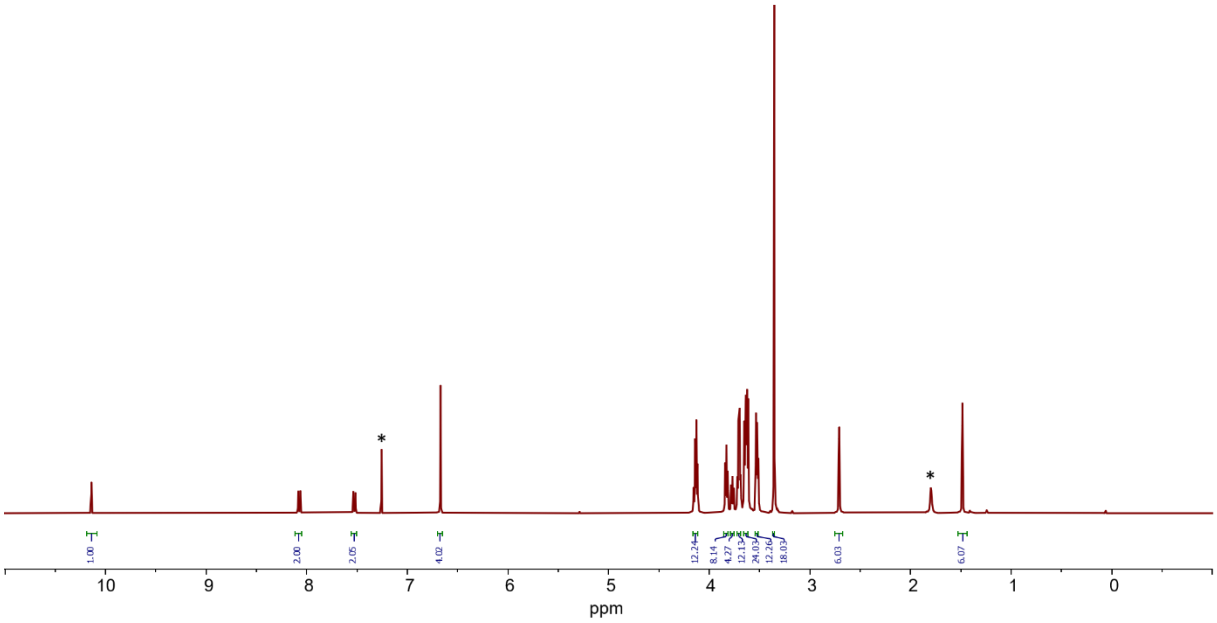

Figure S1: ^{1}H NMR spectrum of compound **1** (298 K, 400 MHz, $CDCl_3$).

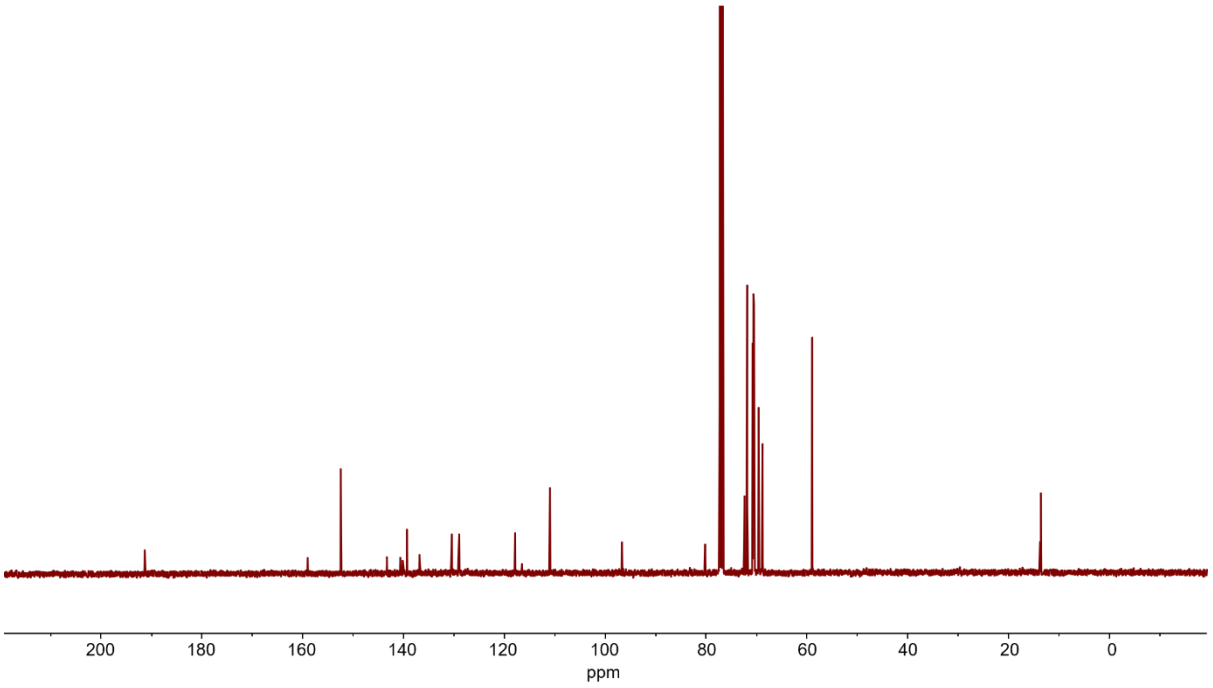

Figure S2: ^{13}C NMR spectrum of compound **1** (298 K, 100 MHz, $CDCl_3$).

Compound **2**

Compound **5** (43 mg, 0.04 mmol, 1 eq.); CuI (2 mg) and $Pd(PPh_3)_4$ (10 mg) were dissolved in a mixture of distilled THF and NEt_3 (25 mL, 3:2, V:V) and stirred at room temperature under a nitrogen atmosphere for 20 minutes. Phenylacetylene (0.1 mL, 93 mg, 0.9 mmol. 23 eq.) was added dropwise. Afterwards the reaction mixture was heated to 323 K and stirred for 12 hours. After cooling to room temperature, the solvent was removed under reduced pressure and the crude product was purified by column chromatography (SiO_2, DCM/MeOH 9:1) and GPC ($CHCl_3$) to give compound **2** as a purple solid.

Yield: 26.0 mg, 0.025 mmol, 63%.

^{1}H NMR: (298 K, 400 MHz, $CDCl_3$): δ = 10.14 (s, 1H); 8.08 (d, *J* = 8.1 Hz, 2H); 7.56-7.51 (m, 2H); 7.48-7.42 (m, 2H); 7.53 (d, *J* = 8.1 Hz, 2H); 6.67 (s, 2H); 4.17-4.11 (m, 6H); 3.86-3.81 (m, 4H); 3.79-3.75 (m, 2H); 3.73-3.68 (m, 6H); 3.66-3.61 (m, 12H); 3.55-3.51 (m, 6H); 3.38-3.35 (m, 9H); 2.72 (s, 3H); 2.71 (s, 3H); 1.50 (s, 3H); 1.49 (s, 3H) ppm.

^{13}C NMR: (298 K, 100 MHz, $CDCl_3$): δ = 191.5; 159.3; 159.2; 152.6; 143.5; 143.4; 140.8; 140.4; 139.5; 137.0; 131.4; 130.7; 130.6; 129.2; 128.5; 128.4; 123.3; 118.1; 111.1; 97.0; 96.8; 81.3; 80.4; 77.4; 72.5; 72.0; 70.9; 70.8; 70.7; 70.6; 69.7; 69.0; 59.2; 14.0; 13.9; 13.8; 13.7 ppm. (note that between δ = 71.0 and 70.5 ppm multiple signals corresponding to the glycol chains overlap, preventing a clear identification of all peaks)

HR-MS (ESI in $MeOH/CHCl_3$): *m/z* calculated for $[M+Na]^+$ = 1061.47557; found = 1061.47625.

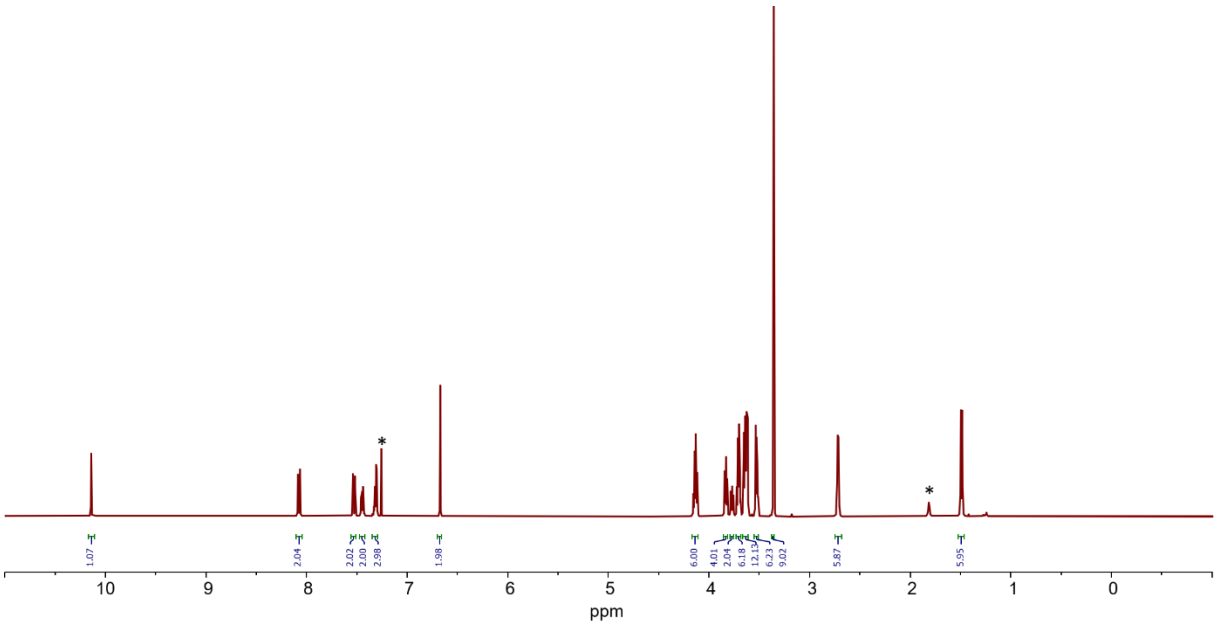

Figure S3: ^{1}H NMR spectrum of compound **2** (298 K, 400 MHz, $CDCl_3$).

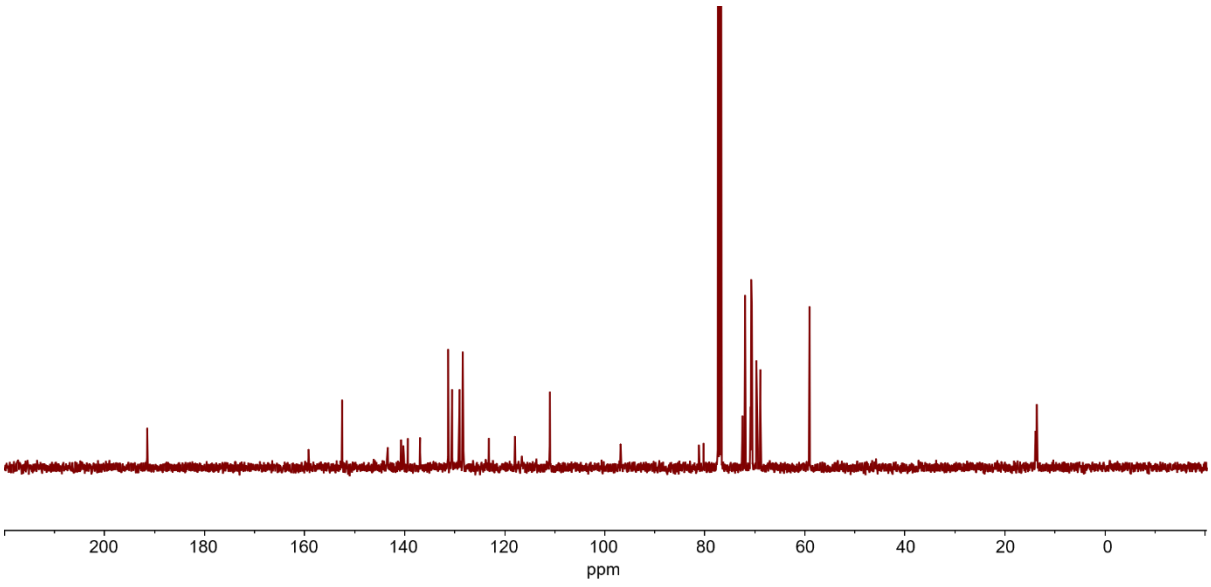

Figure S4: ^{13}C NMR spectrum of compound **2** (298 K, 100 MHz, $CDCl_3$).

Supplementary Figures

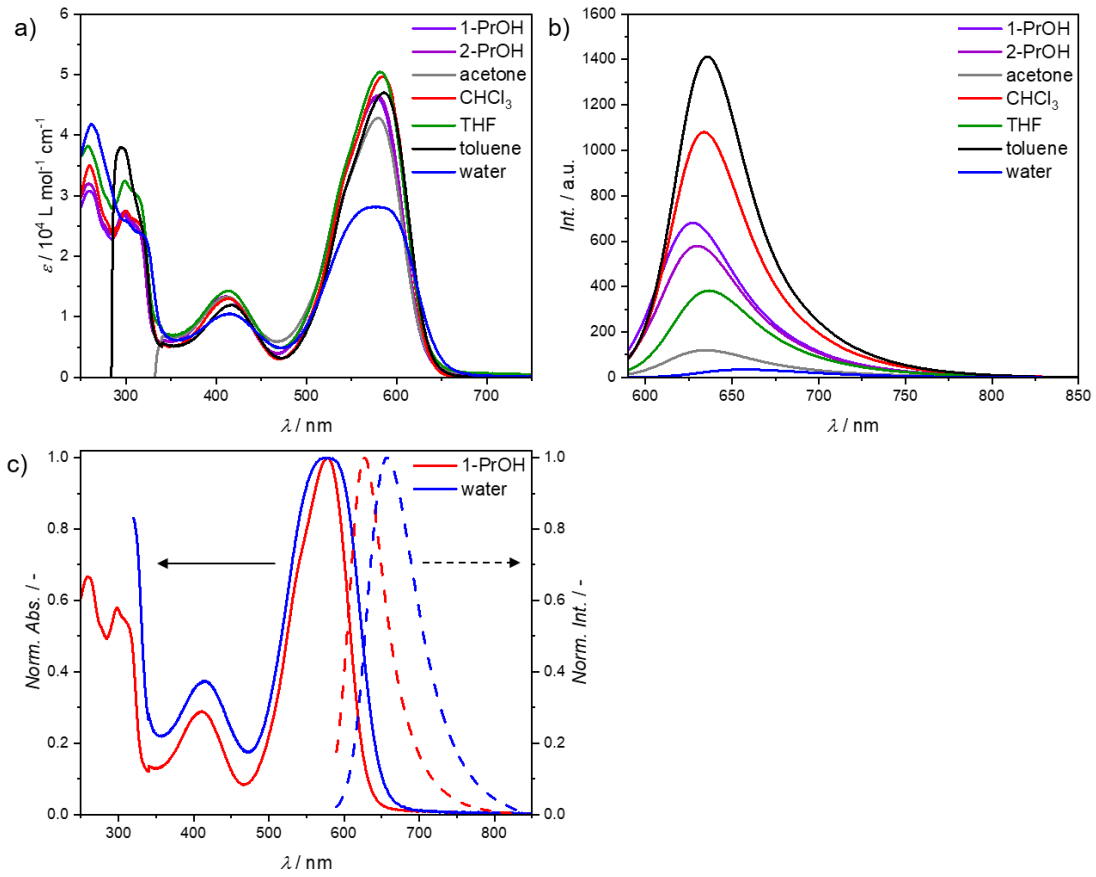

Figure S5: Solvent-dependent UV/Vis (a) and photoluminescence (b) spectra of **1** (c = 10^{-5} M) at T = 293 K. c) Comparison between absorption and luminescence spectra in the molecularly dissolved (1-PrOH, red) and the self-assembled state (water, blue).

Table S1: Summary of the spectroscopic properties of **1** in different solvents.

solvent	$\lambda_{S0\text{-}S1}$ / nm	$\varepsilon_{S0\text{-}S1}$ / $10^4 \cdot L \cdot mol^{-1} \cdot cm^{-1}$	$\lambda_{S0\text{-}S2}$ / nm	λ_{em} / nm	$\Delta\lambda$ / cm^{-1}
1-PrOH	578.0	4.62	411.4	627.0	1352.0
2-PrOH	579.2	4.66	412.2	630.0	1392.2
acetone	579.0	4.28	412.6	634.8	1518.2
$CHCl_3$	584.4	4.97	414.6	633.8	1333.7
THF	581.0	5.04	413.8	637.0	1513.1
toluene	585.0	4.70	417.6	635.6	1360.8
water	573.2	2.82	414.6	657.8	2243.7

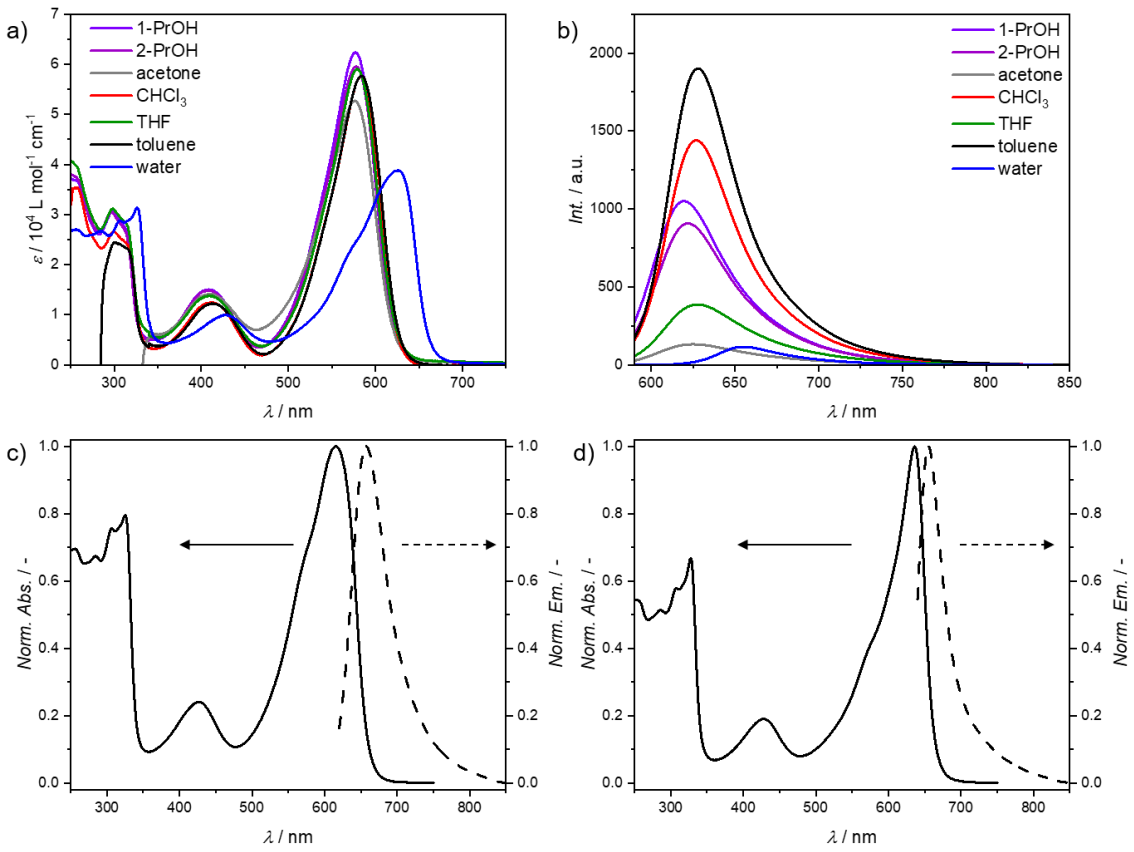

Figure S6: Solvent-dependent UV/Vis (a) and photoluminescence (b) studies of **2** (c = 10^{-5} M) at T = 293 K. c+d) Comparison between absorption and luminescence spectra in water of a freshly dissolved (c) and an equilibrated solution (d).

Table S2: Summary of the spectroscopic properties of **2** in different solvents.

solvent	$\lambda_{S0\text{-}S1}$ / nm	$\varepsilon_{S0\text{-}S1}$ / $10^4 \cdot L \cdot mol^{-1} \cdot cm^{-1}$	$\lambda_{S0\text{-}S2}$ / nm	λ_{em} / nm	$\Delta\lambda$ / cm^{-1}
1-PrOH	576.8	6.24	408.8	619.4	1192.4
2-PrOH	578.0	5.95	407.8	621.6	1213.5
acetone	576.6	5.27	409.0	625.4	1353.3
$CHCl_3$	583.2	5.76	410.6	627.0	1197.8
THF	578.6	5.90	406.6	627.6	1349.4
toluene	583.8	5.76	413.4	628.0	1202.6
water (fresh)	615.8	6.08	425.6	657.4	1027.6
water (aged)	636.0	8.39	426.0	655.0	456.1

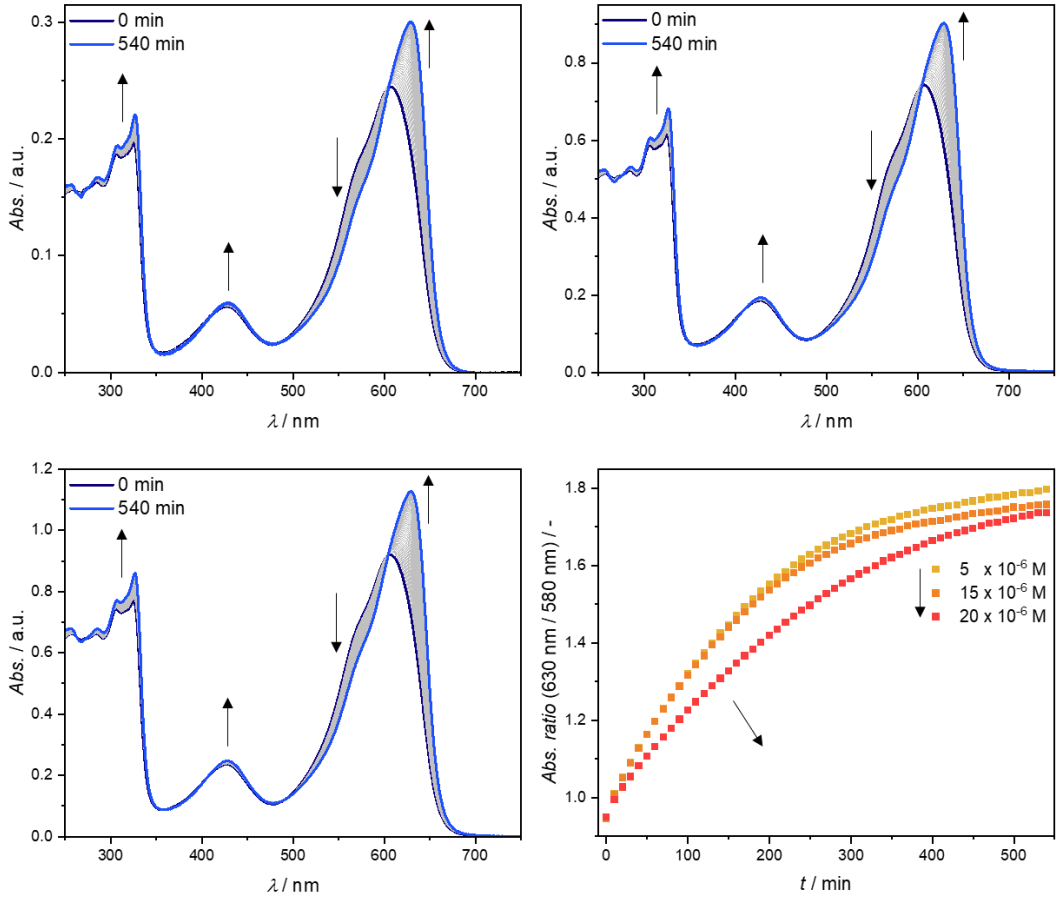

Figure S7: Time-dependent UV/Vis spectra of **2** (c = 5 x 10^{-6} M (a); c = 15 x 10^{-6} M (b); c = 20 x 10^{-6} M (c)) at T = 293 K after freshly dissolving a solid sample in pure water with the changes in the absorbance ratio between λ = 630 and 580 nm plotted against the time, highlighting the formation of a transient kinetic off-pathway species immediately after sample preparation. Arrows indicate the spectral changes upon increasing time (a-c) and concentration (d) respectively.

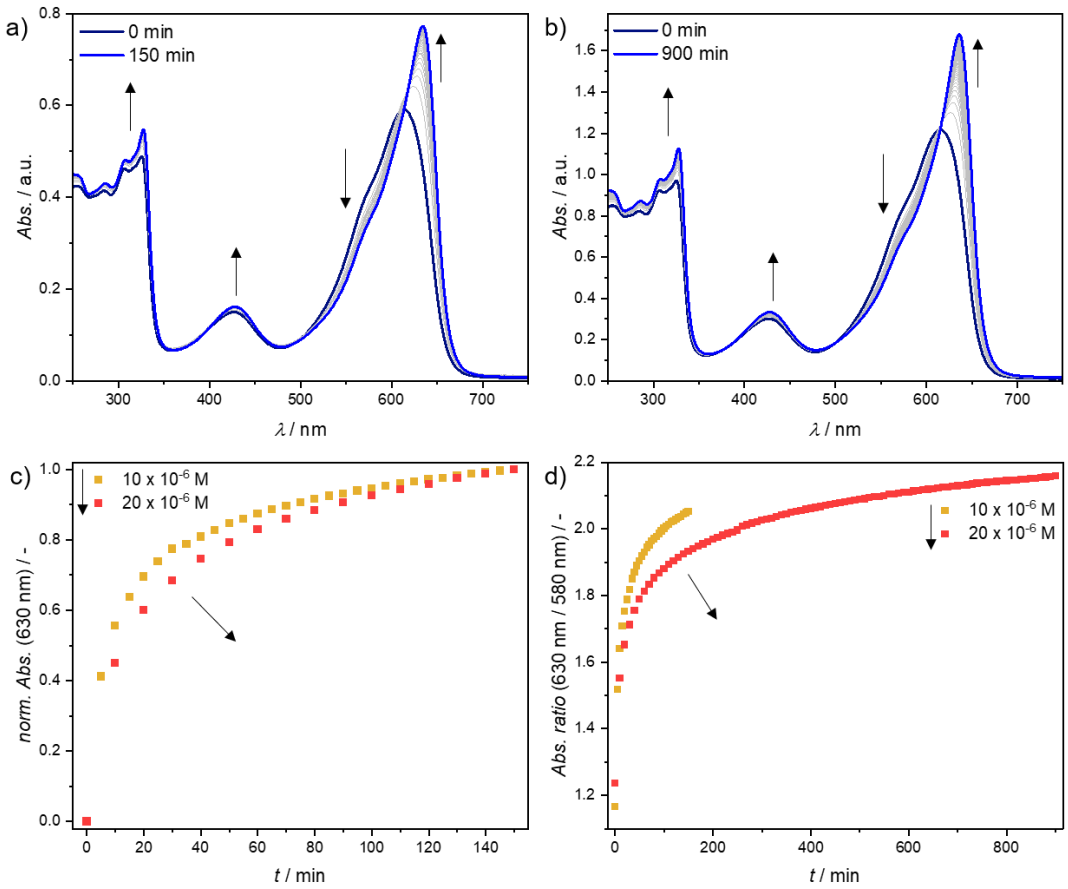

Figure S8: Time-dependent UV/Vis spectra of **2** (c = 10 x 10^{-6} M (a) and c = 20 x 10^{-6} M (b)) at T = 308 K after freshly dissolving a solid sample in pure water with the normalized changes in absorbance at λ = 630 nm (c) and the changes in the absorbance ratio between λ = 630 and 580 nm (d) plotted against the time. Arrows indicate the spectral changes upon increasing time (a+b) and concentration (c+d) respectively.

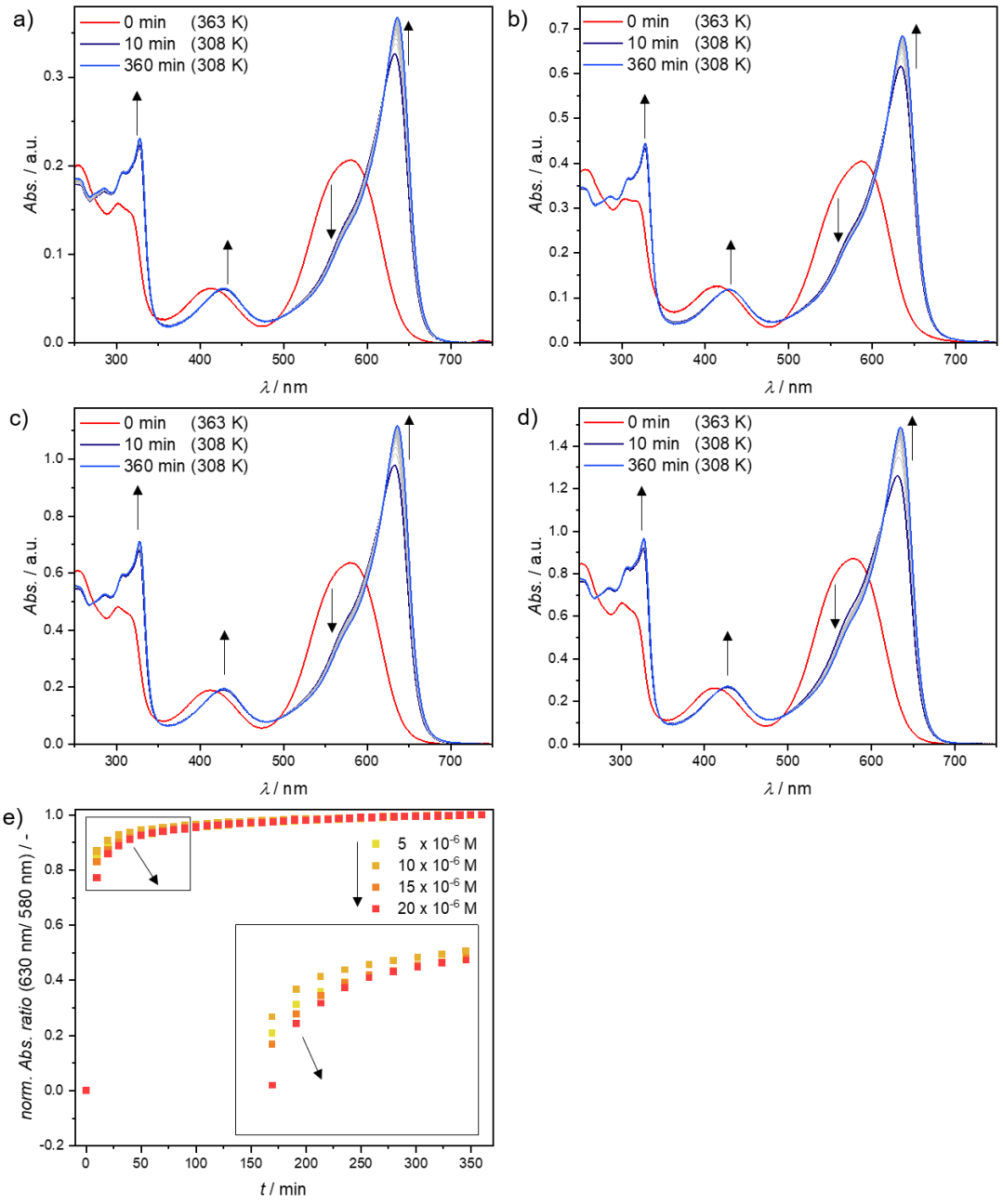

Figure S9: Time-dependent UV/Vis spectra of **2** (c = 5 x 10^{-6} M (a); c = 10 x 10^{-6} M (b); c = 15 x 10^{-6} M (c); c = 20 x 10^{-6} M (d)) at T = 308 K after freshly cooling a hot solution in pure water (10 min equilibration at T = 363 K) with the normalized changes in the absorbance ratio between λ = 630 and 580 nm (e) plotted against the time. Arrows indicate the spectral changes upon increasing time (a-d) and concentration (e) respectively.

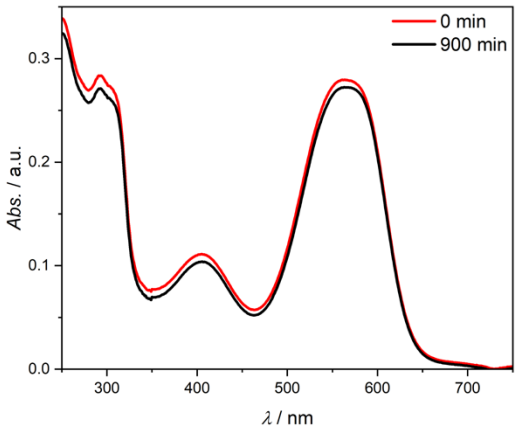

Figure S10: Time-dependent UV/Vis spectra of **1** (c = 10^{-5} M) at T = 293 K, revealing the stability of Agg**1**$_{RT}$ over time.

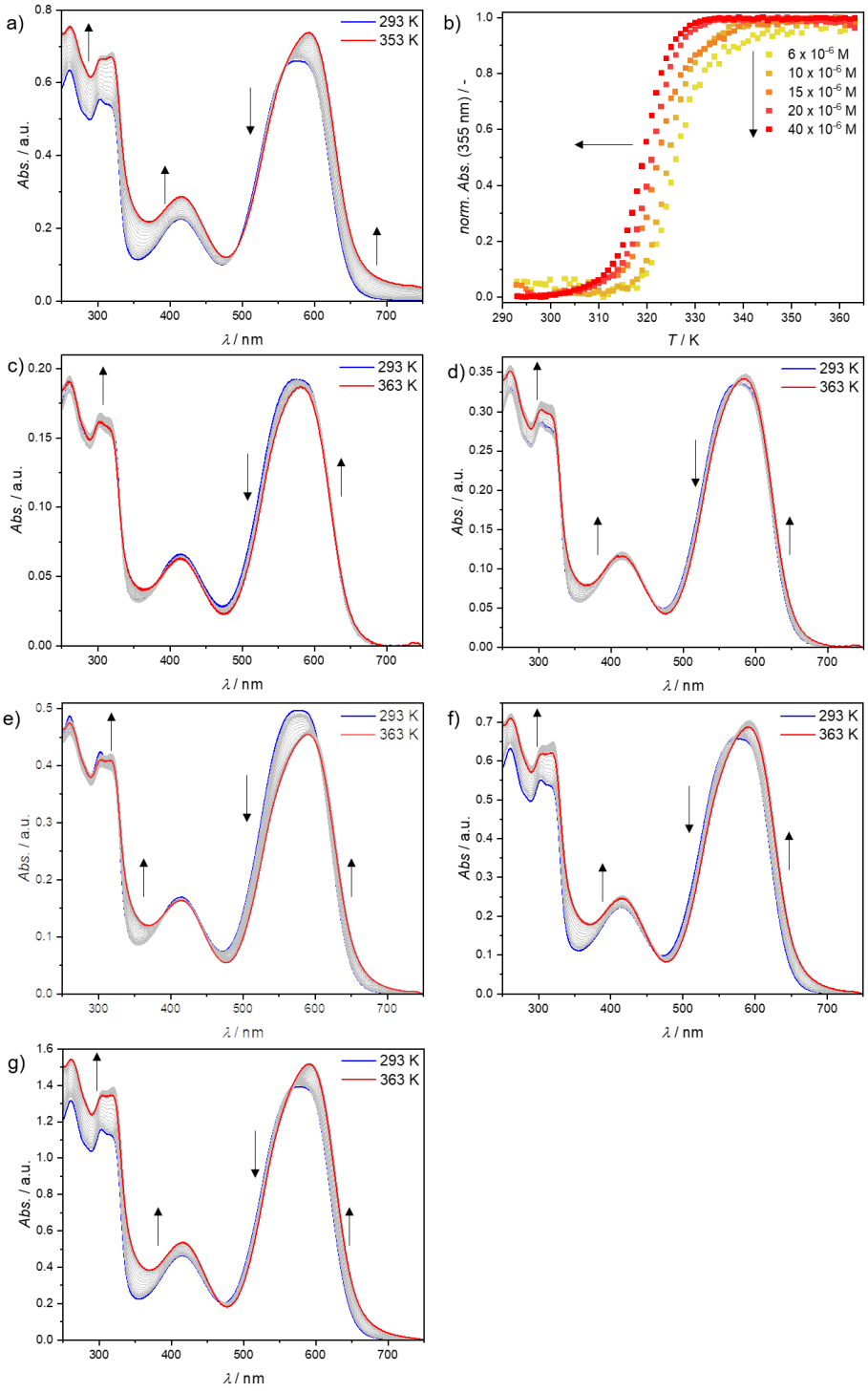

Figure S11: Temperature-dependent UV/Vis spectra of **1** (c = 20 x 10^{-6} M) between T = 353 K and 293 K (a) with the normalized changes in absorbance at λ = 355 nm plotted for various concentrations (b). c-g) Density-corrected temperature-dependent UV/Vis spectra of **1** (c = 6 x 10^{-6} M (c); c = 10 x 10^{-6} M (d); c = 15 x 10^{-6} M (e); c = 20 x 10^{-6} M (f); c = 40 x 10^{-6} M (g)) between T = 353 K and 293 K. Arrows indicate the spectral changes with increasing temperature (a;c-g) and increasing concentration (b) respectively.

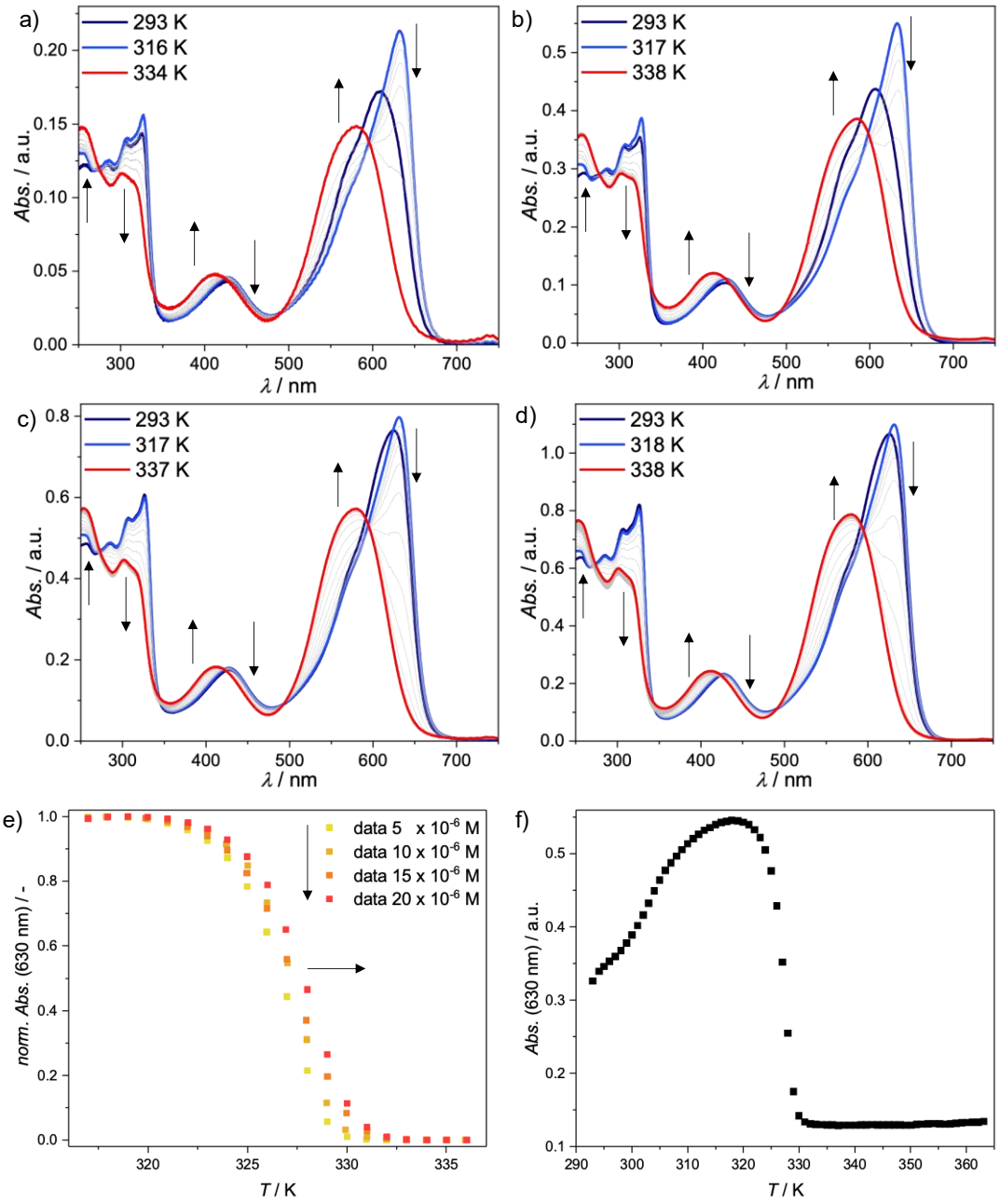

Figure S12: Temperature-dependent UV/Vis spectra of **2** (c = 5 x 10^{-6} M (a); 10 x 10^{-6} M (b); 15 x 10^{-6} M (c); 20 x 10^{-6} M (d)) between T = 316 K and 338 K with the normalized changes in absorbance at λ = 630 nm plotted against the temperature (e). f) The change in absorbance at λ = 630 nm plotted against the temperature between T = 293 K and 363 K at a concentration of c = 10 x 10^{-6} M reveals an initial equilibration period at low temperatures prior to the disassembly process. Arrows indicate the spectral changes upon increasing temperatures (a-d) and increasing concentration (e) respectively.

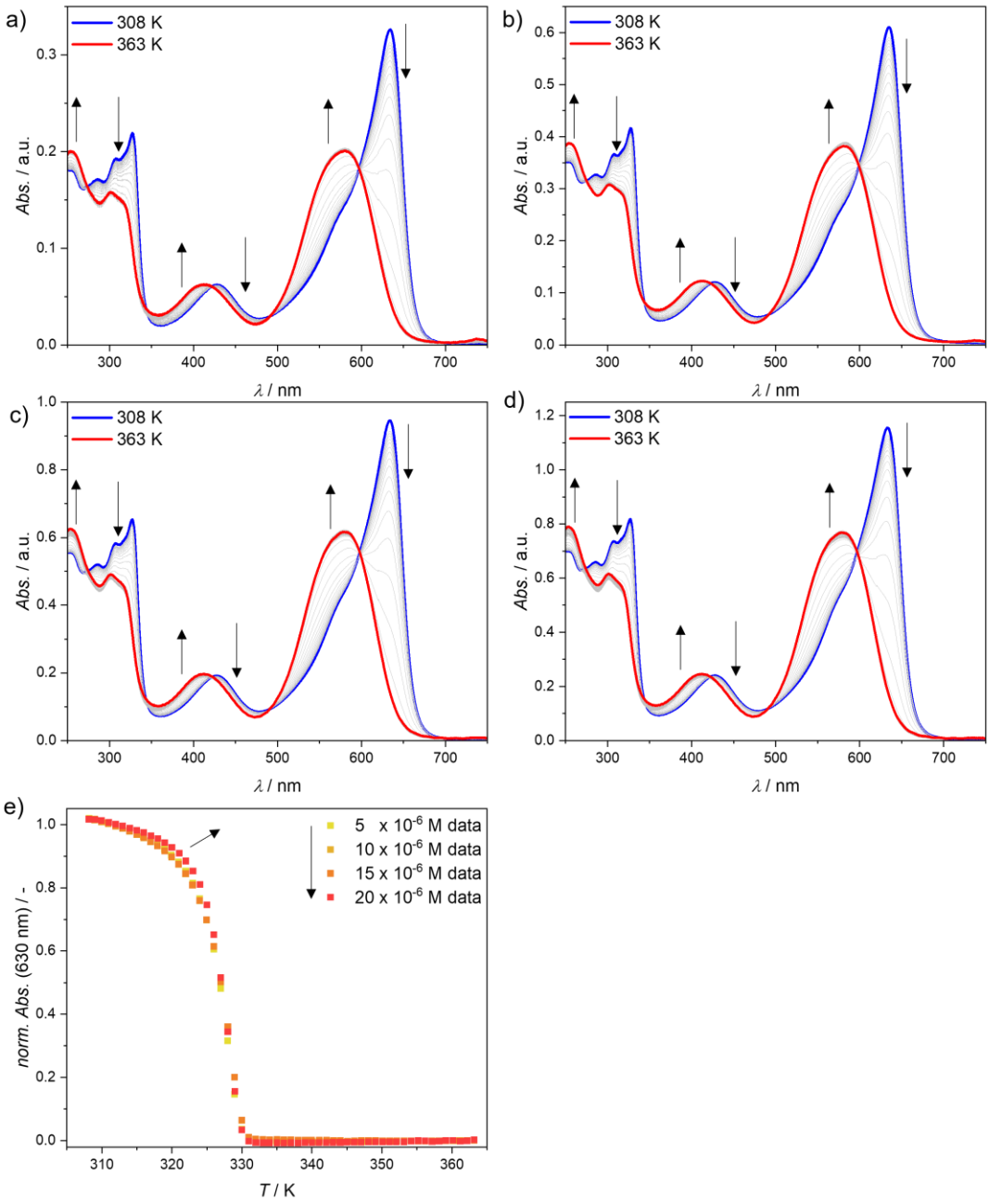

Figure S13: Temperature-dependent UV/Vis spectra of **2** at various concentrations (c = 5 x 10^{-6} M (a); c = 10 x 10^{-6} M (b); c = 15 x 10^{-6} M (c); c = 20 x 10^{-6} M (d)) between T = 293 K and 363 K with the normalized change in absorbance at λ = 630 nm plotted against the temperature (e). Arrows indicate the spectral changes upon increasing temperatures (a-d) and concentration (e) respectively. All measurement solutions were treated according to the thermal equilibration protocol shown in Fig. S9.

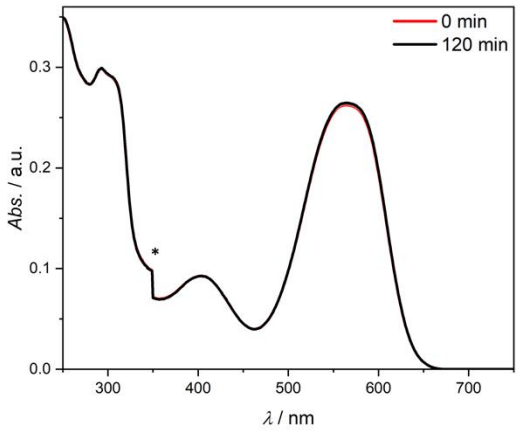

Figure S14: Time-dependent UV/Vis spectra of **1** (c = 10^{-5} M) at T = 293 K. The sample was heated to 363 K for 10 minutes prior to the data acquisition. The first spectrum was recorded immediately after the target temperature was reached and reveals the instantaneous formation of Agg**1**$_{RT}$ after cooling. The asterisk denotes an instrumental artifact.

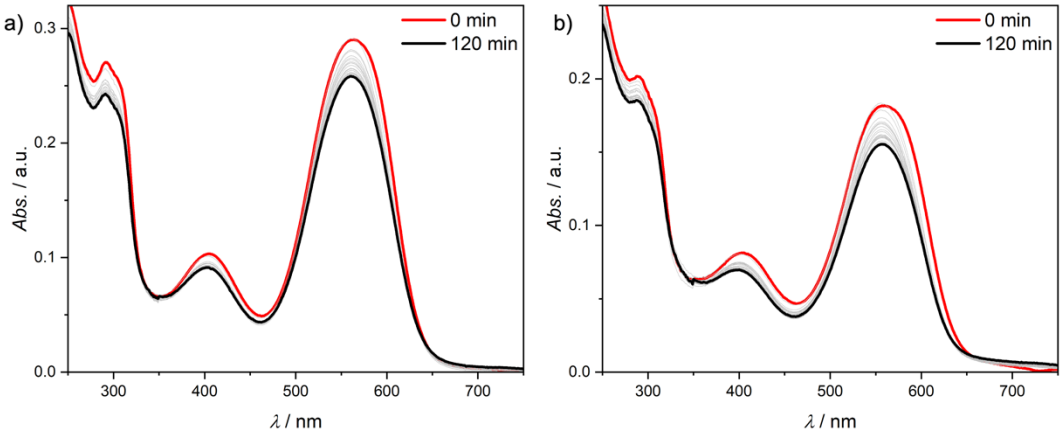

Figure 15: Time-dependent UV/Vis spectra of **1** (a, c = 10^{-5} M) and **2** (b, c = 10^{-5} M) at T = 363 K. The spectra reveal a complete transformation of Agg**1**$_{RT}$ and Agg**2**$_{RT}$ into Agg**1**$_{HT}$ and Agg**2**$_{HT}$ within the first 10 minutes after starting the experiment.

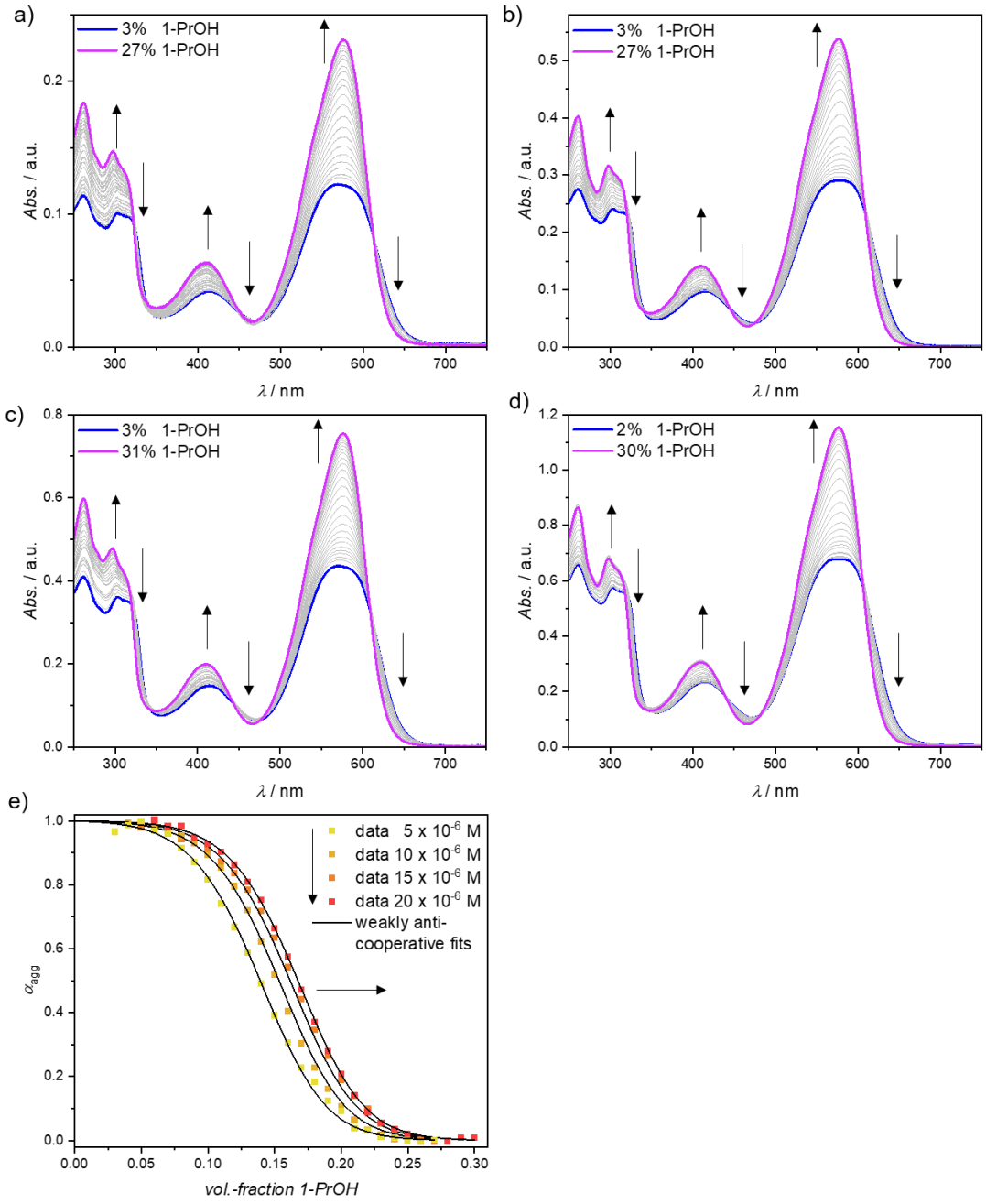

Figure S16: Solvent-dependent UV/Vis spectra of **1** (c = 5 x 10^{-6} M (a); c = 10 x 10^{-6} M (b); c = 15 x 10^{-6} M (c); c = 20 x 10^{-6} M (d)) using water as poor solvent and 1-PrOH as denaturing agent at T = 293 K with the aggregation parameter (α_{agg}) plotted against the volume fraction of 1-PrOH (e). The data was fitted to the solvent-dependent model using a global fitting approach.[3] Arrows indicate the spectral changes with increasing volume fraction of 1-PrOH (a-d) and increasing concentration (e), respectively.

Table S3: Thermodynamic parameters derived from fitting the denaturation curves of **1** in water/1-PrOH to the solvent-dependent model using a global fitting approach.[3]

ΔG^0 / kJ·mol^{-1}	ΔG^0 (SD) / kJ·mol^{-1}	m / kJ·mol^{-1}	m (SD) / kJ·mol^{-1}	σ
-43.9	0.2	119.0	3.1	1.9

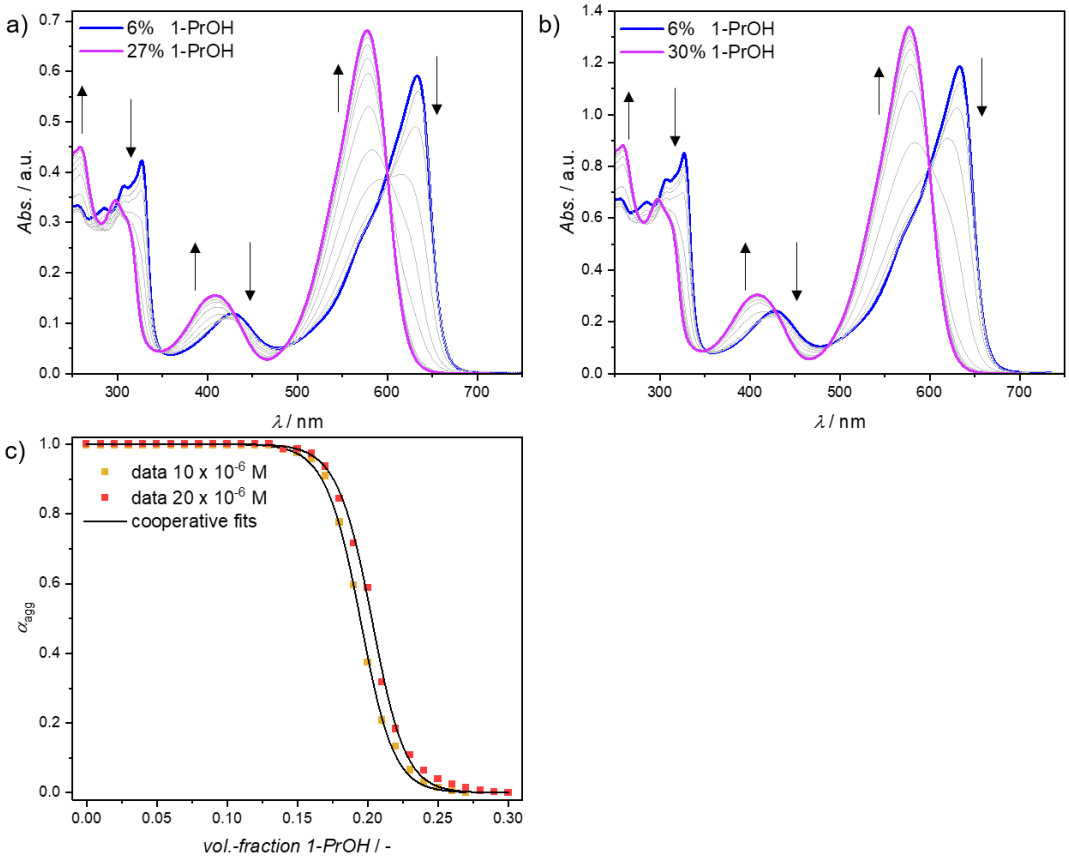

Figure S17: Solvent-dependent UV/Vis spectra of **2** (c = 10 x 10^{-6} M (a) and c = 20 x 10^{-6} M (b)) using water as poor solvent and 1-PrOH as denaturing agent at T = 293 K with the aggregation parameter (α_{agg}) plotted against the volume fraction of 1-PrOH (c). The data was fitted to the solvent-dependent model using a global fitting approach.[3] Arrows indicate the spectral changes with increasing volume fraction of 1-PrOH.

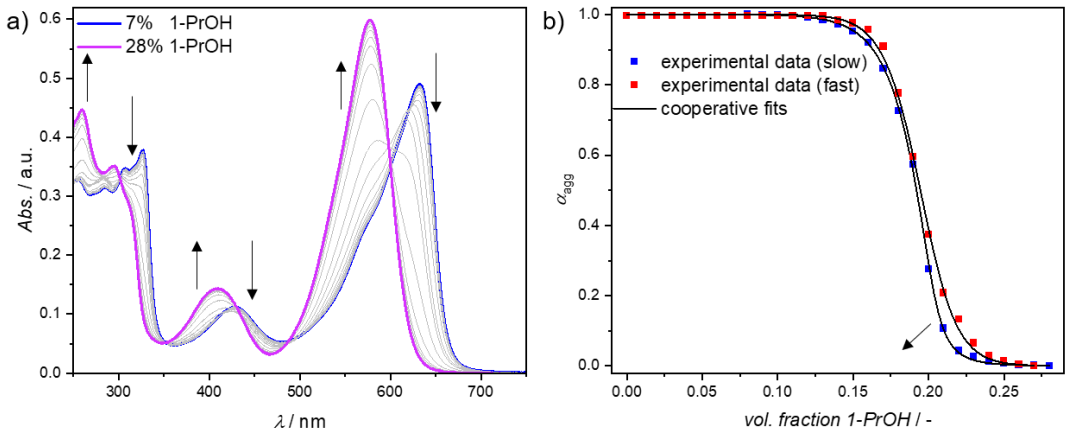

Figure S18: Solvent-dependent UV/Vis spectra of **2** (c = 10 x 10^{-6} M) using water as poor solvent and 1-PrOH as denaturing agent at T = 293 K with the aggregation parameter (α_{agg}) plotted against the volume fraction of 1-PrOH, with the data from an experimental procedure using faster addition of 1-PrOH for reference. The data was fitted to the solvent-dependent model.[3] Arrows indicate the spectral changes with increasing volume fraction of 1-PrOH and decreasing addition rates of 1-PrOH, respectively. Data interval: addition of 1% 1-PrOH every 5 minutes for the fast and every 10 minutes for the slow addition rate.

Table S4: Thermodynamic parameters derived from fitting the denaturation curves of **2** in water/1-PrOH to the solvent-dependent model using an individual fitting approach.

Method	ΔG^0 / kJ·mol^{-1}	ΔG^0 (SD)/ kJ·mol^{-1}	m / kJ·mol^{-1}	m (SD) / kJ·mol^{-1}	σ / 10^{-2}
Fast	-67.4	1.80	206.0	11.0	68.7
Slow	-48.0	0.84	103.0	4.8	4.0

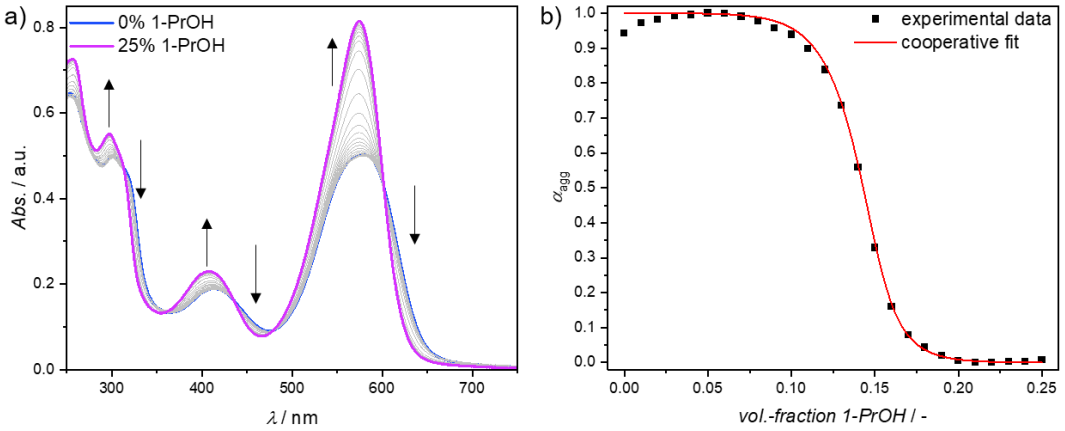

Figure S19: a) Solvent-dependent UV/Vis spectra of **2** (c = 20 x 10^{-6} M) at T = 338 K using water as poor solvent and 1-PrOH as denaturing agent respectively. b) The aggregation parameter derived from the spectra in (a) plotted against the amount of 1-PrOH fitted to the solvent-dependent model.[3] Arrows indicate the spectral changes upon increasing the amount of 1-PrOH. Although the data could be accurately reproduced using the solvent-dependent model, a thermodynamic analysis is precluded due to a partial phase separation of both solvents at this temperature, observed with the naked eye.

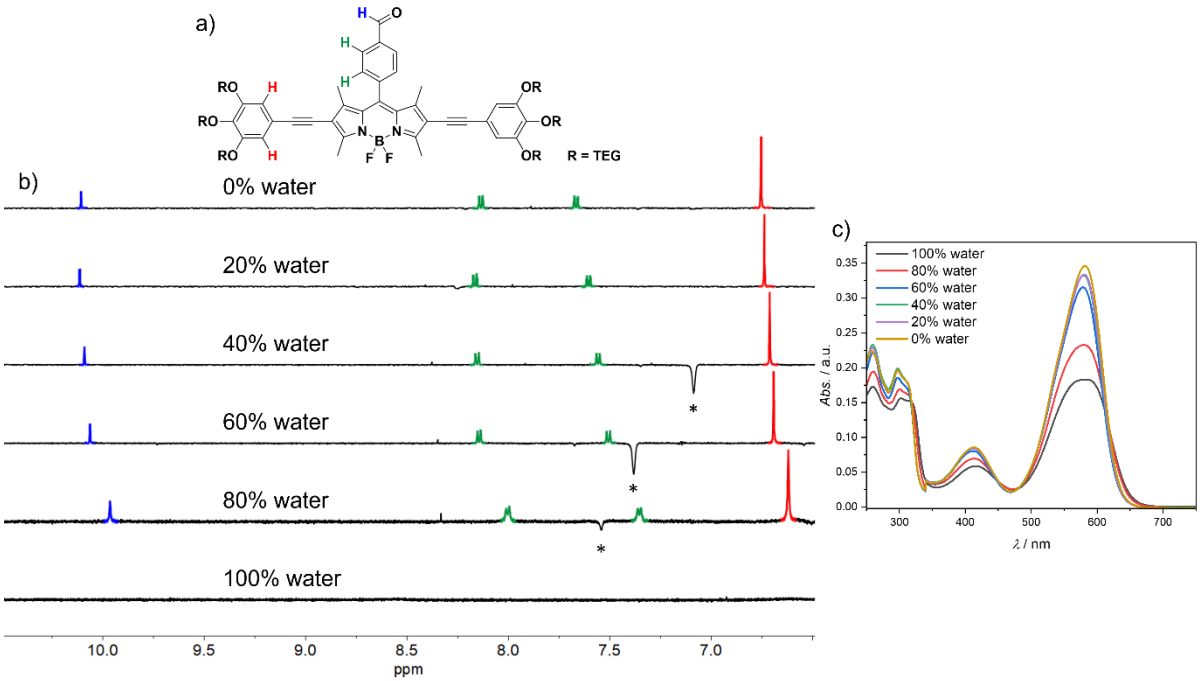

Figure S20: a) Molecular structure of **1**. b) Partial ^{1}H NMR spectra of **1** (c = 5 x 10^{-4} M, T = 293 K), using the colour scheme indicated in (a) using binary mixtures of D_2O and THF-d_8. Asterisks indicate instrumental artifacts. c) UV/Vis spectra of the same solutions as used in (b).

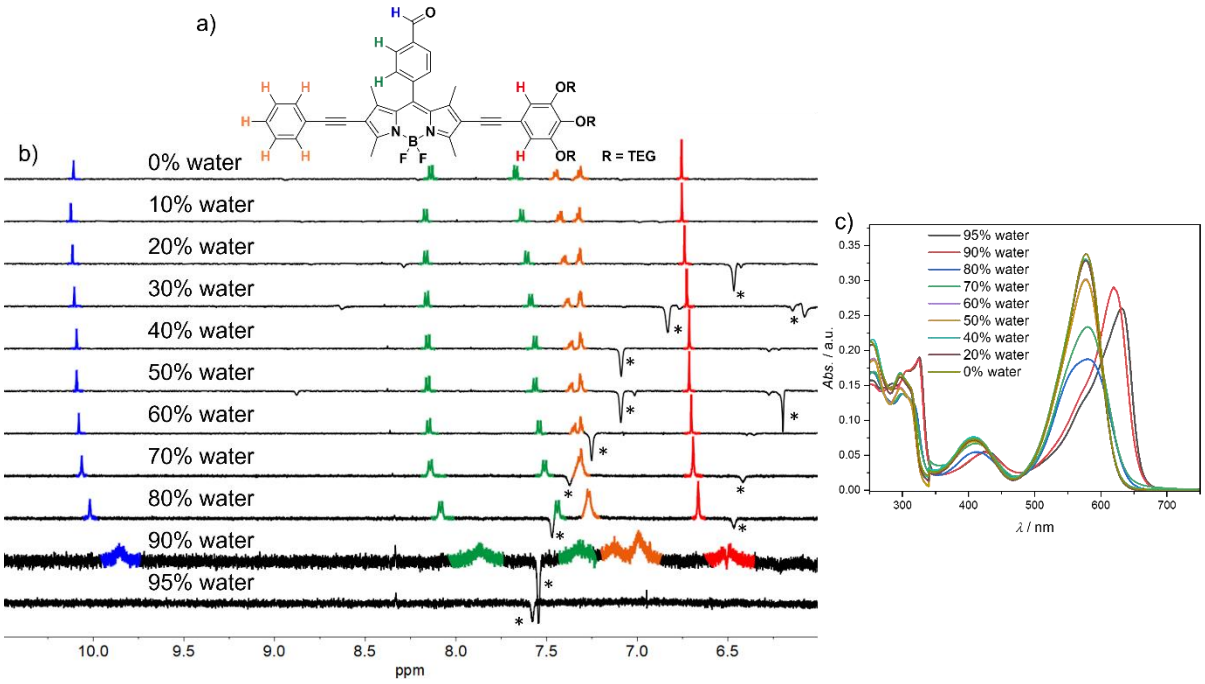

Figure S21: a) Molecular structure of **2**. b) Partial ^{1}H NMR spectra of **2** (c = 5 x 10^{-4} M, T = 293 K), using the colour scheme indicated in (a) using binary mixtures of D_2O and THF-d_8. Asterisks indicate instrumental artifacts. c) UV/Vis spectra of the same solutions as used in (b).

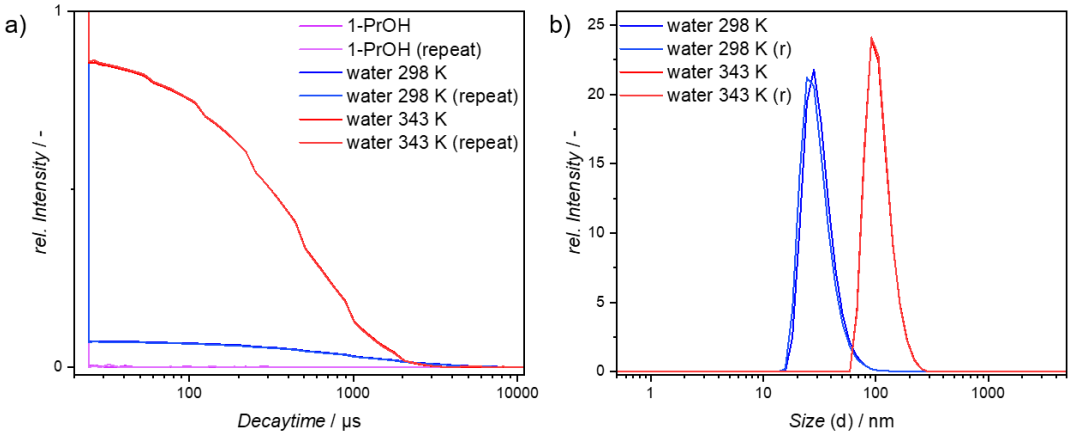

Figure S22: Temperature-dependent DLS studies of **1** (c = 2 x 10^{-5} M) in water using a sample in 1-PrOH as reference, highlighting the heating-induced self-assembly as indicated by UV/Vis. a) Correlation functions; b) Number size distribution functions. The observed increase in the correlation function, combined with the shift in the hydrodynamic size intensity distribution matches well with the increased optical density previously detected in temperature-dependent UV/Vis studies.

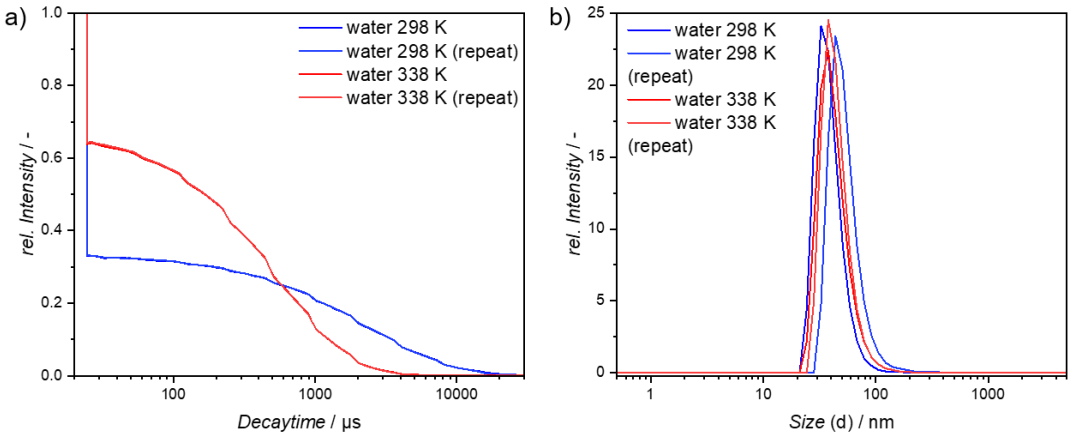

Figure S23: Temperature-dependent DLS studies of **2** (c = 20 x 10^{-6} M) in water, highlighting the heat-induced change in self-assembly as indicated by UV/Vis. a) Correlation functions; b) Number size distribution functions.

It should be noted that the data at T = 298 K should be interpreted with caution due to the overlap of the aggregate absorption maximum (λ = 635 nm) and the DLS laser emission (λ = 633 nm). As such, any light scattering may be perturbed by photoluminescence of the aggregates upon excitation. Accordingly, the observed auto-correlation and size distribution functions should be viewed as an additional hint towards the formation of (relatively) extended supramolecular architectures, as also indicated by supplementary microscopic analysis (*vide infra*) and the specific size distribution profiles should not be analysed in isolation.

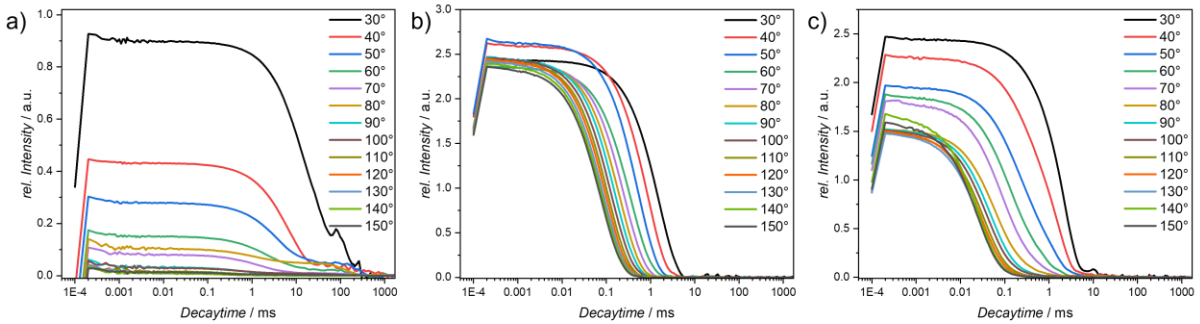

Figure S24: Angle-dependent DLS spectra of **1** (c = 2 x 10^{-5} M) at T = 298 K (a) and 343 K (b) and of **2** (c = 2 x 10^{-5} M; T = 343 K; c), indicating a relatively small structure of Agg**1**$_{RT}$ in solution, while Agg**1**$_{HT}$ and Agg**2**$_{HT}$ show characteristic spectra of larger structures matching the microscopic analysis (*vide infra*).

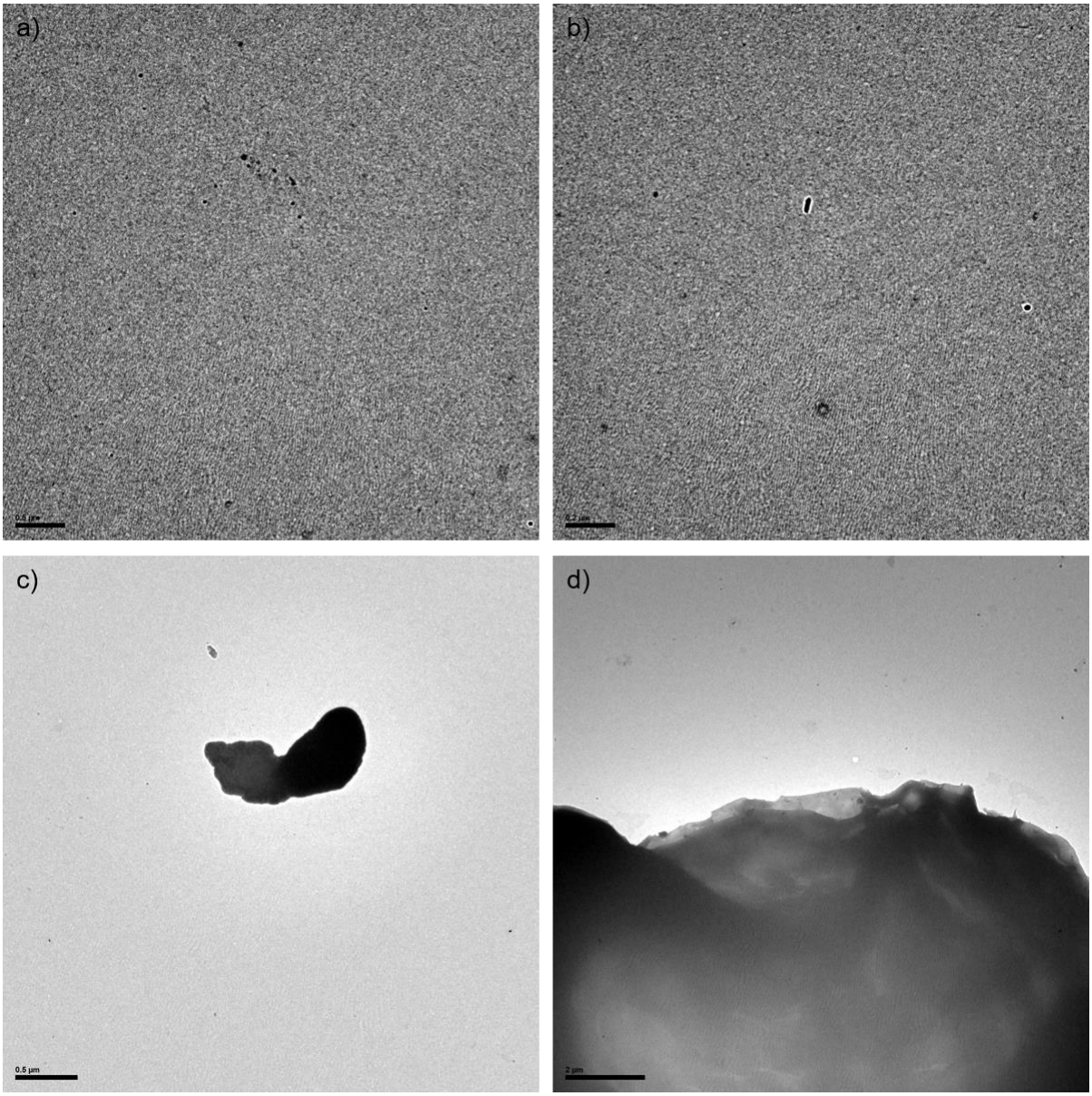

Figure S25: TEM micrographs of **1** (c = 20 x 10^{-6} M) at T = 298 K (a+b) and 338 K (c+d), revealing small spherical particles and sheet-like structures, respectively. The sheets formed by **1** at high temperatures may show an increased tendency to bundle together due to the sample preparation technique. Scale bars correspond to 0.5 (a+c); 0.2 (b) and 2 µm (d).

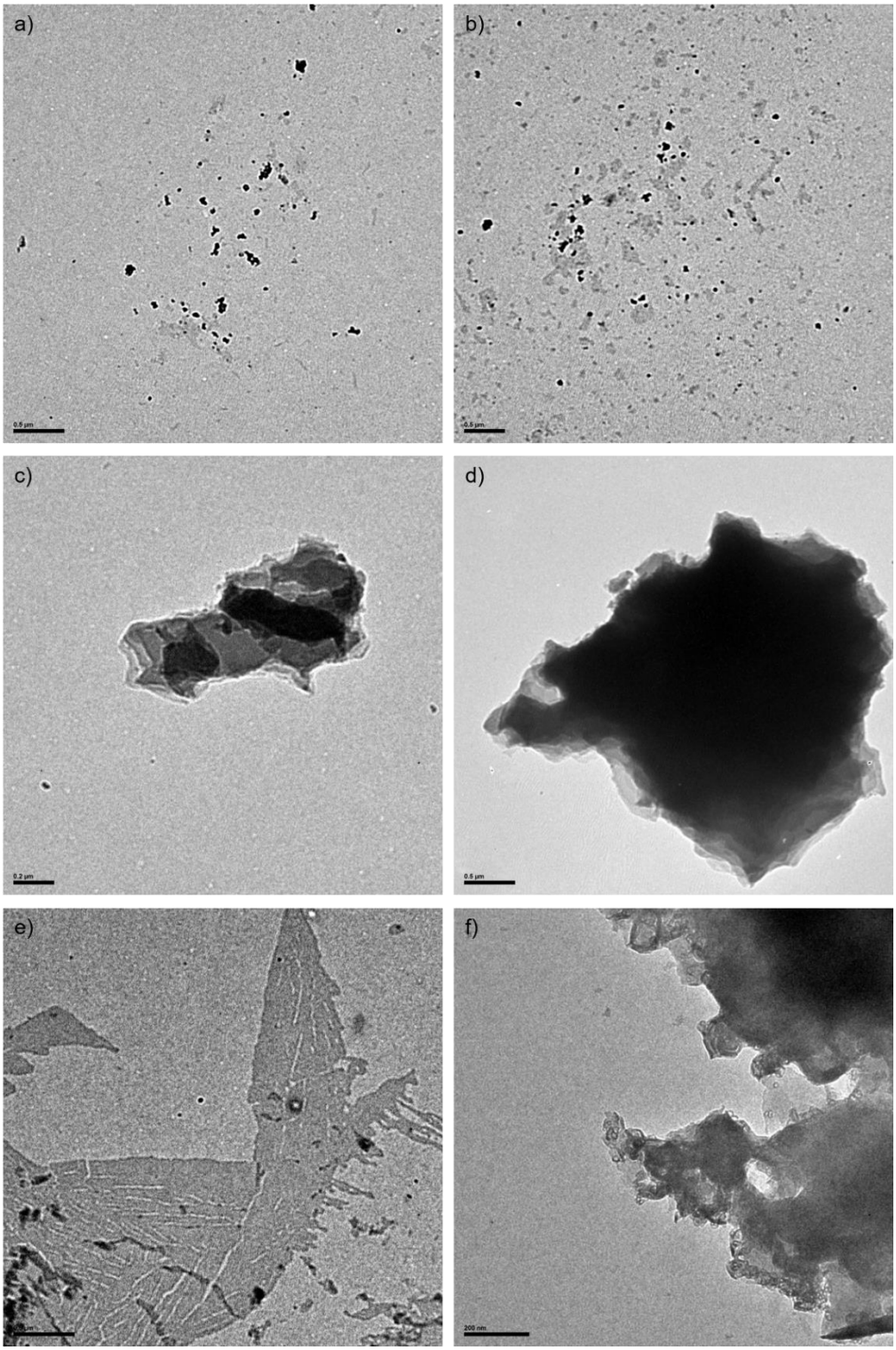

Figure S26: TEM micrographs of **2** (c = 20 x 10^{-6} M) at T = 298 K freshly after preparing (a+b) and after the thermal equilibration protocol (c+d) and at T = 338 K (e+f), revealing small spherical particles and sheet-like structures respectively. The sheets formed by **2** after equilibration and at high temperatures may show an increased tendency to bundle together due to the sample preparation technique. Scale bars correspond to 0.5 (a,b,d+e); 0.2 (c) and 200 µm (f).

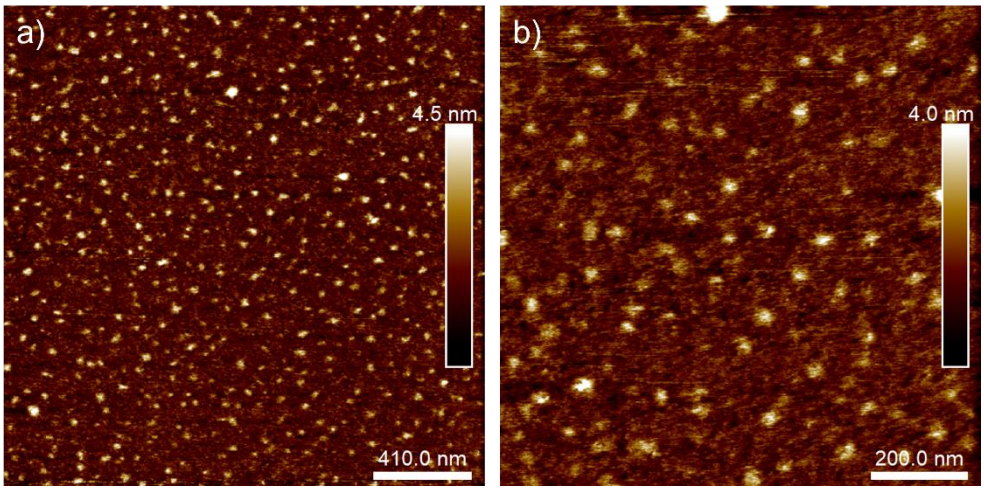

Figure S27: AFM micrographs of Agg**1**$_{RT}$ (c = 2 x 10^{-5} M) in pure water.

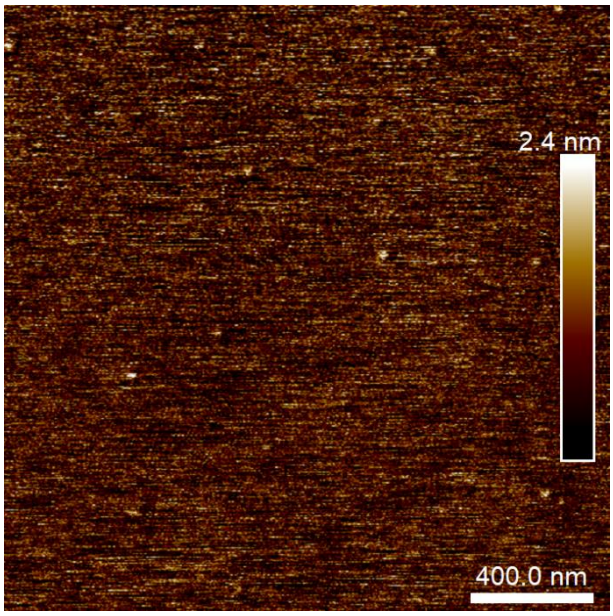

Figure S28: AFM micrographs of Agg**2**$_{Kin}$ (c = 2 x 10^{-5} M) in pure water.

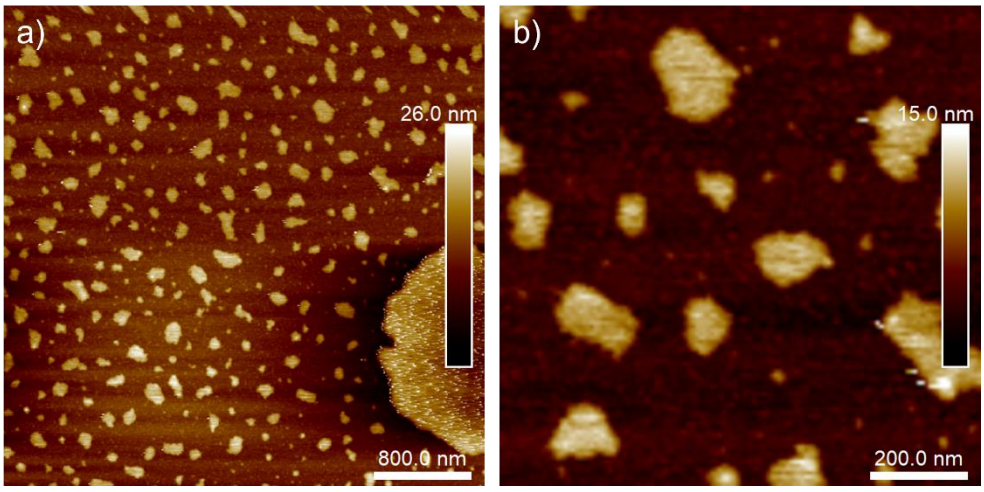

Figure S29: AFM micrographs of Agg**2**$_{RT}$ (c = 2 x 10^{-5} M) in pure water.

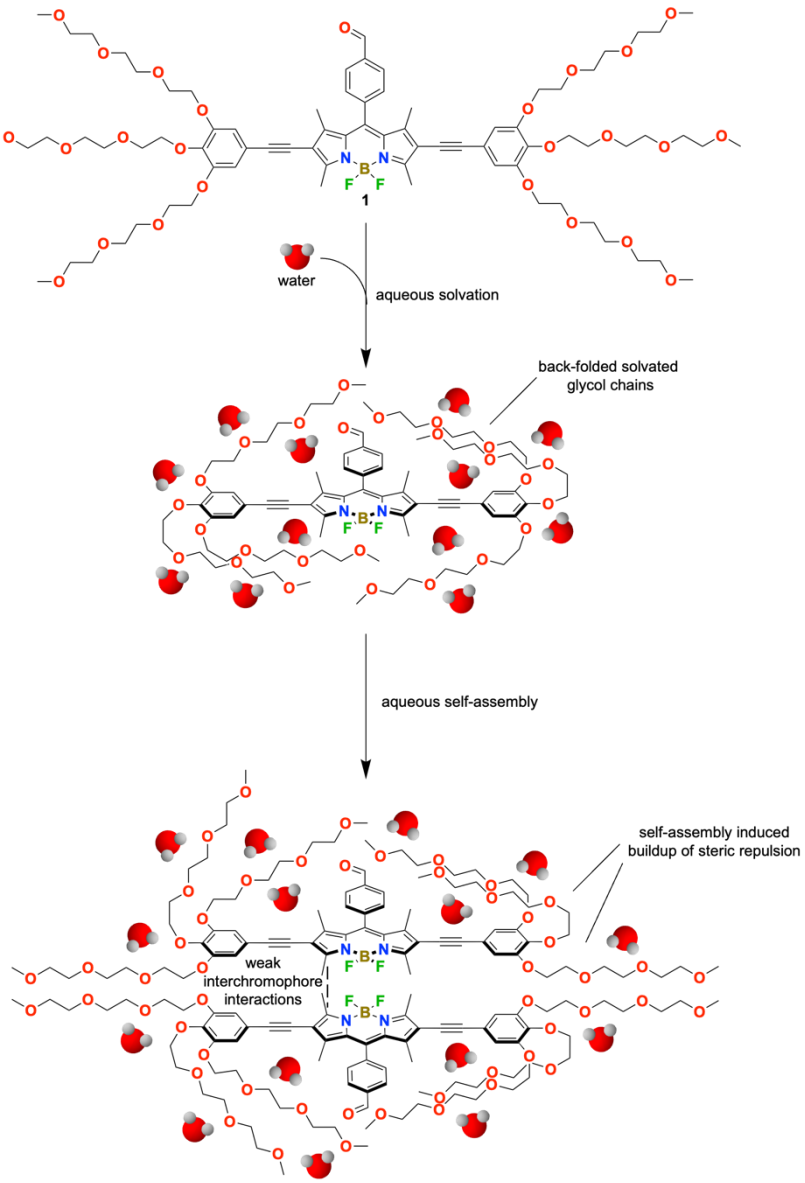

Figure S30: Proposed supramolecular packing mode of Agg**1**$_{RT}$. For visual clarity the proposed structure is limited to a dimer.

Combining the results from spectroscopic and microscopic analysis allows us to derive a probable supramolecular packing mode for Agg**1**$_{RT}$ (Fig. S30). In addition, by comparing the molecular structure of **1** with other organic chromophores investigated in the context of aqueous self-assembly, we can explain key properties of the resulting assemblies. It has been well documented, that organic chromophores equipped with solubilizing glycol chains show a back-folding of the solvated glycol chains upon aqueous solvation, driven by solvophobic effects.[4-6] As a consequence of the relatively high steric demand of these back-folded chains, aggregates formed by this conformation show only weak exciton coupling, which is consistent with the behaviour observed during UV/Vis absorption spectroscopy (Fig. 2a).[4] Additionally, the continuous build-up of steric demand upon further growth is a reasonable explanation for the observed weakly anti-cooperative self-assembly mechanism of **1** (Figs. 4c+d).[7-9] Due to the weak interchromophore interactions upon assembly the obtained supramolecular architectures lack a preferred direction of growth leading to the formation of relatively isotropic spherical particles as shown by AFM and TEM analysis (Figs. 5a, S25 and S27).

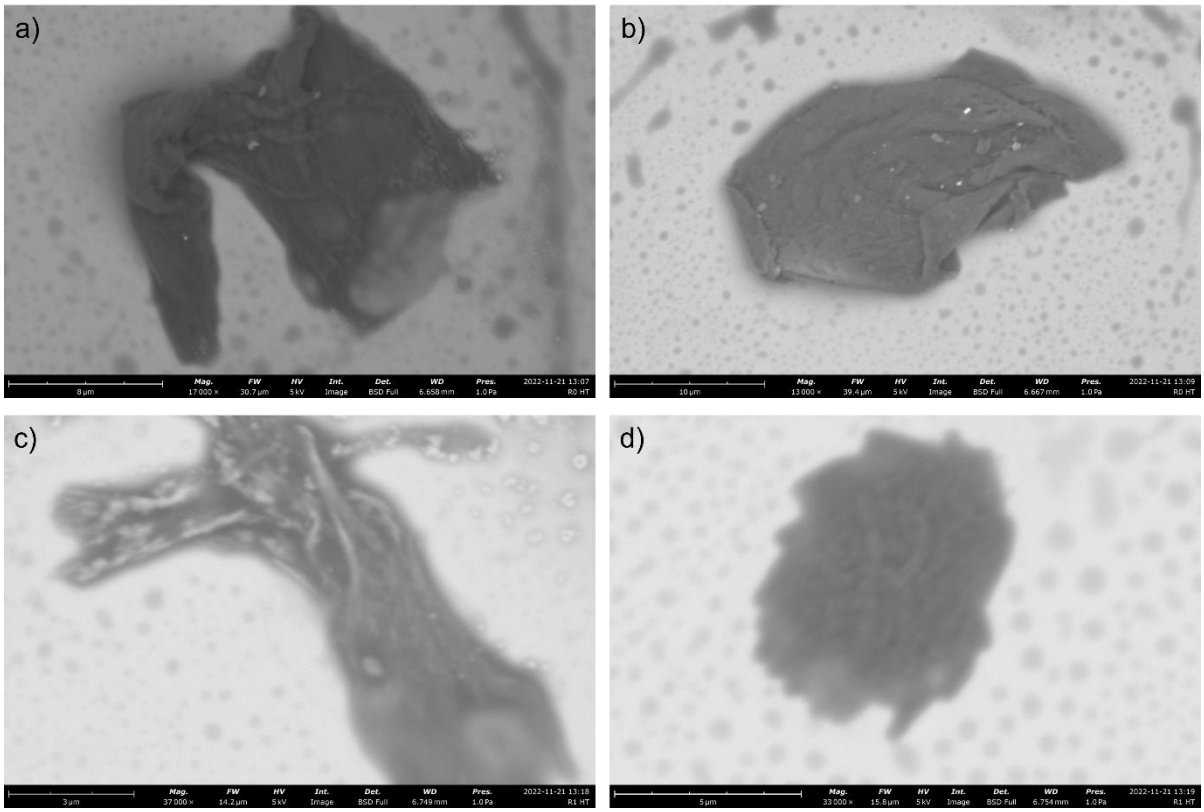

Figure S31: SEM micrographs of Agg$\mathbf{1}_{HT}$ (a+b) and Agg$\mathbf{2}_{HT}$ (c+d) obtained from spin-coating small volume fractions (10 µL) of solutions of **1** and **2** in pure water (c = 2 x 10^{-5} M) at T = 343 K onto a silicon substrate.

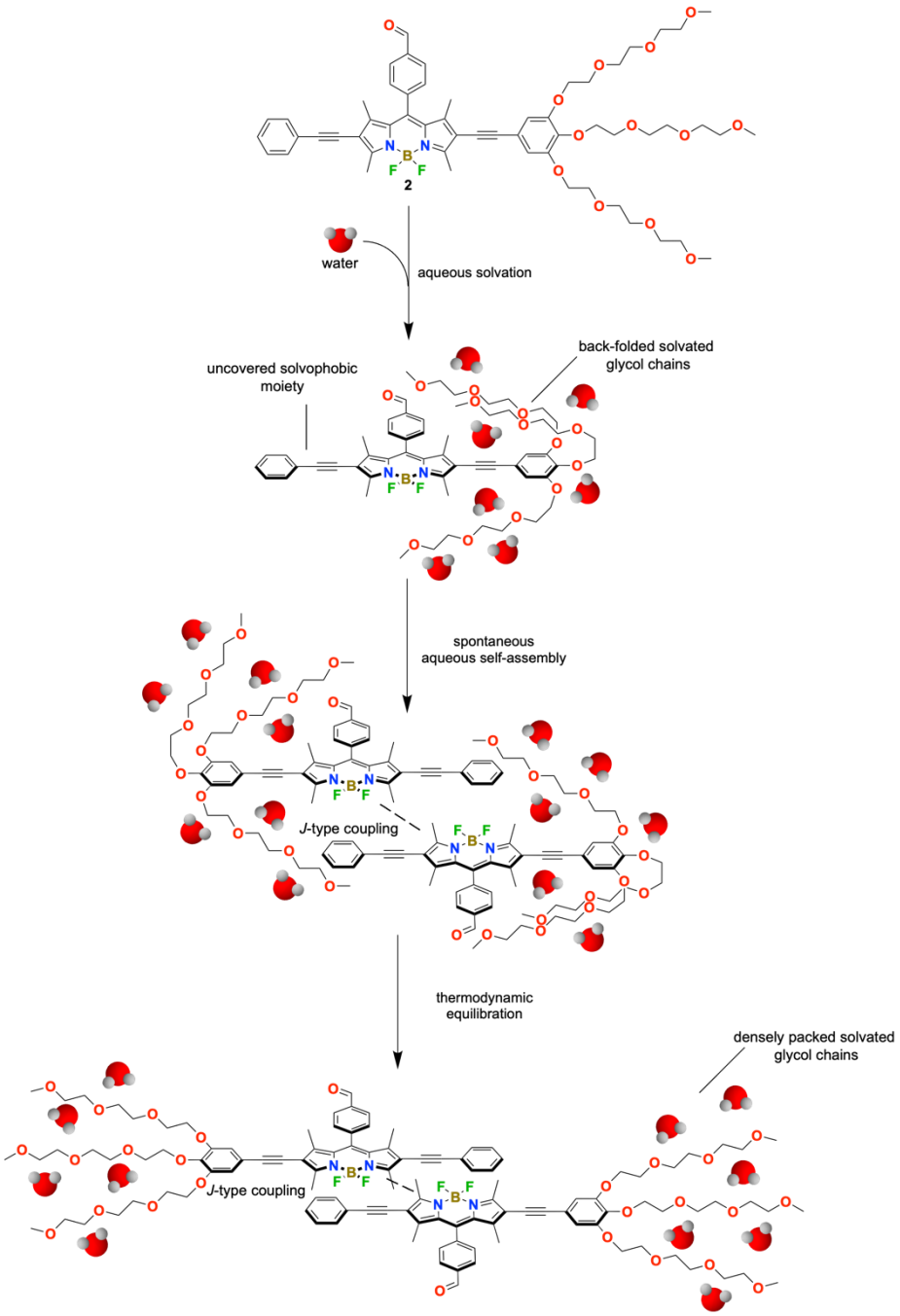

Figure S32: Proposed supramolecular packing mode of Agg**2**$_{RT}$ and Agg**2**$_{Kin}$. For visual clarity the proposed structure is limited to a dimer.

Combining spectroscopic and microscopic analysis of the different assembled states of **2** allows us to propose plausible supramolecular packing modes (Fig. S32). In analogy to the aqueous solvation of **1**, we propose a back-folding of the solubilizing glycol chains driven by solvophobic interactions.[4-6] In contrast to the solvation of **1** this intramolecular configuration exposes the phenylethinylene moiety at the opposite periphery of the molecule to the aqueous media. In order to minimize these unfavourable interactions, an anti-parallel arrangement of the chromophores driven by dipole-dipole repulsion of the aldehyde groups and steric repulsion of the backfolded glycol chains appears reasonable.[10,11] This arrangement results in a *J*-type exciton coupling between the chromophores which is consistent with UV/Vis absorption spectroscopy (Figs. 2b+c). Additionally, as the assembly process is likely driven by solvophobic interactions in a kinetically controlled manner, the resulting

morphologies could be visualized as isotropic spherical particles (Figs. 5b, S26 and S28). Upon thermal equilibration, these kinetically controlled assemblies transform into thermodynamically more stable architectures with pronounced interchromophore interactions (Figs. 2b and S7-S9). We propose a close antiparallel packing with a large translational offset to be the origin of this phenomenon (Fig. S32). This packing results in a densely packed glycol layer covering the surface of the assemblies, which matches the apparently defect-free surface of the architectures visualized by AFM (Figs. 5c and S29). Further this packing serves as a reasonable explanation for the uncovered cooperative assembly process (Figs. 4e+f, S17 and S18), as the nucleation of such an assembly is expected to be unfavourable in aqueous media (low $K_{nucl.}$), but yield a high enthalpic gain upon growth (high $K_{el.}$) leading to a low value of σ ($K_{nucl.}$ / K_{el}). Further support for this assignment stems from the extracted height profile (Fig. 5c), which matches the proposed large translational offset combined with a dense glycol chain layer.[12]

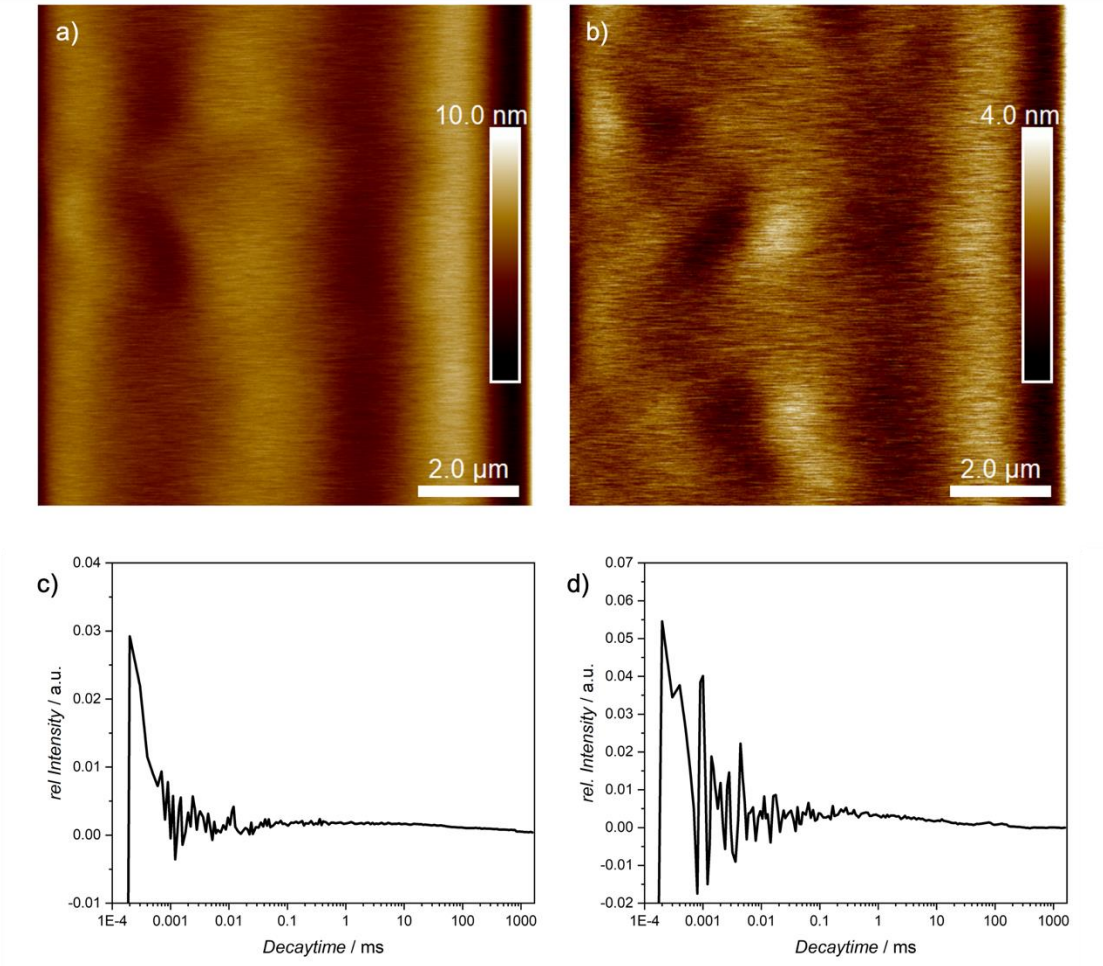

Figure S33: a+b) AFM height images of MICA substrates spin coated with THF solutions of **1** (a, c = 2 x 10^{-5} M) and **2** (b, c = 2 x 10^{-5} M) respectively, revealing the absence of any assembled architectures. c+d) DLS correlation functions of the same solutions used for a (c) and b (d), supporting the absence of self-assembled structures in solution.

References

[1] I. Helmers, B. Shen, K. K. Kartha, R. Q. Albuquerque, M. Lee, G. Fernández, *Angew. Chem. Int. Ed.* 2020, **59**, 5675.

[2] M. Korzec, S. Kotowicz, K. Laba, M. Lapkowski, J. G. Malecki, K. Smolarek, S. Maćkowskian, E. Schab-Balcerzak, *Eur. J. Org. Chem.* 2018, **15**, 1756.

[3] P. A. Korevaar, C. Schaefer, T. F. A. de Greef, E. W. Meijer, *J. Am. Chem. Soc.* 2012, **134**, 13482.

[4] L. Borsdorf, L. Herkert, N. Bäumer, L. Rubert, B. Soberats, P. A. Korevaar, C. Bourque, C. Gatsogiannis, G. Fernández, *J. Am. Chem. Soc.* 2023, **145**, 8882.

[5] P. P. N. Syamala, B. Soberats, D. Görl, S. Gekle, F. Würthner, *Chem. Sci.*, 2019, **10**, 9358.

[6] P. P. N. Syamala, F. Würthner, *Chem. Eur. J.*, 2020, **26**, 8426.

[7] I. Helmers, M. S. Hossain, N. Bäumer, P. Wesarg, B. Soberats, L. S. Shimizu, G. Fernández, *Angew. Chem. Int. Ed.*, 2022, **61**, e202200390.

[8] Y. Dorca, C. Naranjo, G. Ghosh, B. Soberats, J. Calbo, E. Orti, G. Fernández, L. Sánchez, *Chem. Sci.*, 2022, **13**, 81.

[9] K. Cai, J. Xie, Di Zhang, W. Shi, Q. Yan and D. Zhao, *J. Am. Chem. Soc.*, 2018, **140**, 5764.

[10] H. Chen, H. Ye, Y. Hai, L. Zhang and L. You, *Chem. Sci.*, 2020, **11**, 2707.

[11] M. G. Holl, M. D. Struble, M. A. Siegler and T. Lectka, *J. Fluor. Chem.*, 2016, **188**, 126.

[12] I. Helmers, N. Bäumer, G. Fernández, *Chem. Commun.*, 2020, **56**, 13808.